Internal structure and dynamics of stratified flow over sloping topography

Lars Umlauf

Internal structure and dynamics of stratified flow over sloping topography

Habilitationsschrift

zur

Erlangung des akademischen Grades

doctor rerum naturalium habilitatus (Dr. rer. nat. habil.)

der Mathematisch-Naturwissenschaftlichen Fakultät

der Universität Rostock

vorgelegt von;

Lars Umlauf aus Rostock,
geb. am 16. Oktober 1969 in Rüsselsheim

Rostock, den 02. Juli 2012

Contents

Chapter 1

Introduction

When Munk (1966) suggested that the balance between upwelling and downward mixing in the abyssal ocean may be described to first order in form of a simple one-dimensional advection-diffusion equation, he was well aware of the fact that the basin-scale behavior expressed by his model may in fact be the response to localized processes occurring near the boundaries. This is immediately evident for the advection part of Munk's model that describes basin-scale upwelling as the result of deep-water renewal due to bottom gravity currents, propagating down the continental slopes in comparatively narrow boundary layers. Munk (1966) also speculated, based on the rather limited data available at that time, that the lateral boundaries may play a key role also for net basin-scale mixing, which compensates the advective downward transport of fluid on the long-term average.

This point of view was later supported by the results from open-ocean tracer experiments (Ledwell et al., 1993; Ledwell and Hickey, 1995; Ledwell et al., 2000) and direct observations of turbulence microstructure in the abyssal ocean (Toole et al., 1994; Polzin et al., 1997), revealing the unexpectedly low mixing rates of the open ocean, and the presence of mixing hot-spots in the vicinity of topography. Over the last decades, Munk's ideas have been refined but the overall picture, and even the net mixing rates originally inferred from his model, have remained remarkably robust (Munk and Wunsch, 1998; Wåhlin and Cenedese, 2006). The dynamical implications of the inhomogeneous distribution of mixing suggested by these investigations have been summarized by Wunsch and Ferrari (2004), who pointed out that *"the now inescapable conclusion that over most of the ocean significant vertical mixing is confined to topographically complex boundary areas implies a potentially radically different interior circulation than is possible with uniform mixing"*.

Although scales and physical forcing mechanisms are rather different, these basic components of the overturning circulation are completely analogous to the Baltic Sea, one of the primary study areas in this work. Also in the Baltic Sea, deep-water renewal occurs in the

form of bottom gravity currents traveling down the topographic slopes, with the important difference, however, that these flows are triggered by intermittent intrusions of saline (and thus dense) waters from the adjacent North Sea rather than by surface cooling as in the high-latitude ocean (Meier et al., 2006; Meier, 2007; Reissmann et al., 2009). On the long-term average, the downward advection of dense waters due to these inflows is balanced by vertical mixing, which is, similar to the much larger ocean basins, confined to the bottom boundary layers on the slopes as recently shown from the results of a tracer experiment and turbulence microstructure observations in the central Baltic Sea (van der Lee and Umlauf, 2011; Holtermann et al., 2012; Holtermann and Umlauf, 2012).

On even smaller scales, the processes described above have also been observed in lakes that form the focus of the second part of this work. Also here, tracer studies and direct turbulence observations have shown that boundary mixing is the key to basin-scale mixing, controlling energy dissipation and net "vertical" transport of matter and heat (Goudsmit et al., 1997; Wüest and Lorke, 2003; Wain and Rehmann, 2010). However, since the deepest layers in most lakes are ventilated at least once per year by complete overturning, deep-water renewal due to bottom gravity currents plays a much less critical role compared to the ocean. Exceptions are a number of large and deep meromictic lakes that remain stably stratified throughout the year, with the deep layers ventilated mainly by dense waters cascading down the slopes. Examples for this process include the world's deepest lake, Lake Baikal (Killworth et al., 1996; Wüest et al., 2005), and Lake Geneva, one of the largest Western European lakes (Fer et al., 2001). The overall conclusion from this is that the downward transport of fluid in the form of dense bottom currents, and the subsequent upward mixing, constitute two essential components of the basin-scale overturning circulation in the majority of stratified basins, over a large range of scales and for various forcing conditions. Both types of processes have received considerable attention in the past, and will also be central to this work.

The mathematical description of dense bottom currents has mainly been based on the framework of inviscid rotating hydraulics (e.g., Gill, 1977; Killworth, 1992), and more recently also on theories emphasizing the role of frictional effects (Wåhlin, 2004; Darelius and Wåhlin, 2007). So-called stream-tube models combine aspects of both approaches, and have been successfully used to predict the propagation pathways of gravity currents in the presence of topography and entrainment (Smith, 1975; Baringer and Price, 1997b). All of these theories, however, describe gravity currents only as vertically homogeneous near-bottom layers, which completely ignores the internal structure of these flows. Except for a few three-dimensional modeling studies (e.g., Ezer, 2006), the reasons for and dynamical implications of the observed internal variability and structure of bottom gravity currents have received surprisingly little attention. Based on idealized numerical investigations, and an extensive observational program in the Baltic Sea, these issues are the central topic of the first part of this work described in the following Chapter 2.

In the second part, a special type of boundary mixing process, identified a few years ago in the boundary layer of a lake with strong internal seiching activity, will be analyzed. In this process, differential advection leads to gravitationally unstable layers inside the bottom boundary layer (Lorke et al., 2005), with yet unknown implications for the overall dynamics and diapycnal mixing. A similar mechanism, though strongly modified by rotational effects, has also been identified on the ocean (Moum et al., 2004), suggesting that this phenomenon is of some general relevance. Focusing on lakes with small rotational effects, the discussion in Chapter 3 extends a number of recent studies of boundary mixing that take into account the internal structure of the near-bottom layer but ignore the possibility and implications of gravitationally unstable layers and near-bottom convection (e.g., Perlin et al., 2005, 2007; Taylor and Sarkar, 2008).

This work has been funded by the German Research Foundation (DFG) through the projects QuantAS (Quantification of water mass transformation in the Arkona Sea) and ShIC (Shear-induced convection in bottom boundary layers). I am indebted to various colleagues and students that accompanied the extensive field program for the gravity current studies, especially to Hans Burchard, who was also involved in the modeling part of this project, and supported this work in many other ways. I enjoyed the inspiration and reliable collaboration with Lars Arneborg from the University of Gothenburg (Sweden) in the framework of QuantAS, and with Alfred Wüest from the Swiss EAWAG and Andreas Lorke, at that time at the University of Constance, who motivated the modeling investigations of shear-induced convection in lakes. Numerical simulations have been performed with the open-access models GETM (www.getm.eu) and GOTM (www.gotm.net), and Karsten Bolding's continued effort to keep these codes in an excellent state is greatly appreciated.

Chapter 2

Internal structure and dynamics of frictionally controlled gravity currents

2.1 Introduction

Bottom gravity currents passing over a sill or through a topographic constriction are known to form crucial control points for the general overturning circulation in stratified ocean basins. This important class of flows has therefore attracted continuous attention over the past decades of oceanographic research, with some well-investigated examples including the Faroe Bank Channel overflow (Mauritzen et al., 2005; Seim and Fer, 2011), the Mediterranean outflow through the Strait of Gibraltar (Baringer and Price, 1997a), and the Red Sea outflow plume passing through a system of submarine canyons into the Arabian Sea (Peters et al., 2005). Analogous to their large-scale counterparts in the ocean, also in the Baltic Sea the deep water formation process is strongly depending on the transport of water masses associated with dense deep-water inflows. A recent research focus in this area have been the gravity currents passing through topographic constrictions like the Bornholm Channel in the Southern Baltic (Borenäs et al., 2007; Reissmann et al., 2009), the Stolpe Channel in the Baltic Proper (Paka et al., 1998; Zhurbas et al., 2012), and the small-scale channels in the Western Baltic that will be the main topic of this chapter (Umlauf et al., 2007; Umlauf and Arneborg, 2009a). On even smaller spatial scales, usually referred to as "topographic corrugations", field observations (e.g. Foldvik et al., 2004; Sherwin et al., 2008), idealized numerical modeling studies (Liang and Garwood, 1998; Ilıcak et al., 2011), and laboratory experiments (Davies et al., 2006; Wåhlin et al., 2008; Darelius, 2008) have revealed that submarine ridges and canyons are responsible for the effective downward transport of dense

shelf waters that ultimately determines deep-water formation. As will be shown in the following, the Baltic Sea forms a nearly ideal natural laboratory for the investigations of these flows.

The classical description of bottom gravity currents in the vicinity of topographic constrictions follows the framework of rotating hydraulic theory, based on the conservation of potential vorticity and mass, and the Bernoulli equation formulated for a negatively buoyant near-bottom layer (Gill, 1977; Pratt and Lundberg, 1991; Killworth, 1992). Hydraulic theory has proven particularly useful for flows with hydraulic control points, where it allows for the computation of the lateral interface structure and transport capacity from a limited number of upstream parameters (e.g., Pratt, 2004; Lake et al., 2005). However, as already concluded by Pratt (1986) from simple scaling arguments, there is an increasing body of evidence that real oceanic gravity currents are strongly influenced by frictional effects, different from most laboratory experiments and the assumptions of classical hydraulic theory. Bulk momentum budgets constructed from observations (Johnson et al., 1994b; Baringer and Price, 1997a; Astraldi et al., 2001), and direct turbulence measurements (Johnson et al., 1994a; Peters and Johns, 2005, 2006; Umlauf and Arneborg, 2009a) have provided further support for this changing view on dense bottom currents.

These findings have induced a number of attempts to modify the hydraulic equations to incorporate frictional effects (e.g. Pratt, 1986; Johnson and Ohlsen, 1994). Above all, however, they have motivated the development of a new class of models not based any more on the principles of hydraulic theory. These models, usually formulated as a set of layer-integrated equations for a single active near-bottom layer with reduced gravity, assume that the bulk momentum budget in the main flow direction is characterized by a balance between the interfacial pressure gradient and the sum of the bottom and entrainment stresses. This simple balance, sometimes referred to as *frictional control*, implies that any memory of the upstream conditions (e.g., of upstream potential vorticity) is lost, reducing the model geometry to two dimensions in the cross-stream direction. Motivated by observations from the Baltic Sea, Lundberg (1983) has formulated the basic principles in form of a layer-integrated reduced-gravity model, later modified and extended to describe gravity currents passing through different types of submarine canyons (Wåhlin, 2002, 2004) or along ridges (Darelius and Wåhlin, 2007; Darelius, 2008). Models of this type have been reported to provide plausible descriptions of the lateral interface structure and transport capacity of oceanic (Wåhlin, 2004; Borenäs et al., 2007) and laboratory gravity currents (Darelius, 2008; Cuthbertson et al., 2011).

One immediate consequence of frictional control that will be a central point in the following discussion is the emergence of near-bottom and interfacial Ekman transports. These lateral circulation patterns may distort the internal density structure of the gravity current and strongly modify the dynamics. Johnson and Sanford (1992) attributed the cross-channel

density structure and secondary (cross-channel) circulation patterns in the Faroe Bank Channel overflow to this effect, analyzed later in more detail in laboratory experiments (Johnson and Ohlsen, 1994) and idealized numerical simulations (Ezer, 2006). Secondary currents associated with lateral Ekman transports were also invoked by Paka et al. (1998) in order to explain the lateral density structure in the Stolpe Channel, a well-known propagation pathway for bottom gravity currents in the Baltic Sea. As shown below, however, Ekman transports constitute only one, although crucial, component of the secondary circulation such that the existing picture of frictionally controlled gravity current remained incomplete at that time.

The following sections describe some new insights into the complex physics of frictionally controlled, rotating gravity currents, recently gained in the framework of the QuantAS project ("Quantification of water mass transformations in the Arkona Sea"), funded by the German Research Foundation (DFG). Focal area of QuantAS was the Arkona Basin in the Western Baltic, a region well-known for the occurrence of gravity currents with particularly clear and stable signals due to frequently intruding saline waters from the North Sea (Reissmann et al., 2009). QuantAS has combined observations from ship campaigns (e.g., Sellschopp et al., 2006; Umlauf et al., 2007) and numerical investigations (e.g., Burchard et al., 2009; Umlauf et al., 2010) to obtain an integrated view of the dynamics of gravity currents in this important region for water mass transformation. Key component of this study were observations of turbulence parameters that are difficult to obtain in real oceanic gravity currents, and therefore rare. These results have helped understanding the dynamics of larger systems like the well-investigated Faroe Bank Channel overflow at the North Atlantic margin (Fer et al., 2010; Seim and Fer, 2011)

In the following, the scientific background and the contribution of 7 papers that constitute the first part of this work will be briefly summarized. The combined modeling and observational study in Paper 1 by Arneborg et al. (2007) discusses a one-dimensional description of the dynamics of dense bottom currents. Paper 2 by Umlauf et al. (2007) contains the first high-resolution, synoptic measurements of hydrographic and turbulence parameters across a topographically constrained oceanic gravity current. This data set has motivated the analysis of the dynamics of such flows discussed in Papers 3 and 4 by Umlauf and Arneborg (2009a,b). Complementary to these observational studies, in Paper 5 Umlauf et al. (2010) analyze the dynamics of frictionally controlled, rotating gravity currents with the help of idealized numerical simulations. Essential for the correct representation of entrainment in these complex flows was a reliable parametrization of sub-grid scale mixing that is discussed in detail in Paper 6 by Umlauf and Burchard (2005). Some special modeling issues regarding the description of mixing and entrainment in dense bottom gravity currents and other relevant flows in large-scale ocean models are finally discussed by Umlauf (2009) in Paper 7.

2.2 Mathematical description

Based on the assumption that information about the upstream conditions is negligible in frictionally controlled gravity currents, the problem can be described in a two-dimensional configuration. Therefore, in Papers 1-5 an idealized geometry was considered, consisting of a bottom gravity current passing through an infinitely long and deep channel (or along an infinitely long ridge) with constant down-channel tilt, $S_x \ll 1$, rotating at a constant rate, $f/2$, around the vertical axis (Figure 2.1). The down- and cross-channel coordinates are denoted by x and y, respectively, such that the z-axis exhibits a small tilt, S_x, with respect to the vertical. The gravity current is driven by its negative buoyancy relative to the ambient fluid,

$$b = -g\frac{\rho - \rho_\infty}{\rho_0} \,, \tag{2.1}$$

where g denotes the acceleration of gravity, ρ the (potential) density, ρ_0 a constant reference density, and ρ_∞ the density of the ambient fluid for $z \to \infty$. Changes in the down-channel direction are ignored ($\partial/\partial x \equiv 0$) such that the problem becomes two-dimensional in the y-z plane. The main flow direction is thus aligned with the x-axis (Figure 2.1).

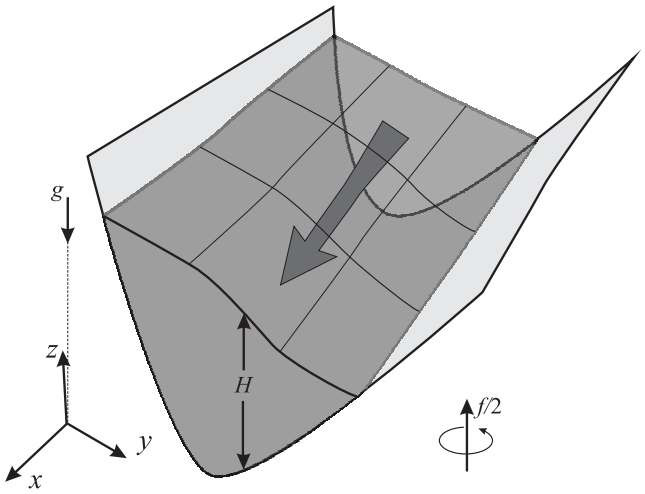

Figure 2.1: (a) Schematic view of a channelized bottom gravity current. The large arrow indicates the direction of the down-channel flow.

2.2.1 Governing equations

Assuming a flow with small aspect ratio, the evolution of the down- and cross-channel velocities, u and v, and the buoyancy, b, is described by the shallow-water version of the Boussinesq equations. In the rotated coordinate system depicted in Figure 2.1, assuming a small down-channel tilt $S_x \ll 1$, it can be shown that these equations are of the following

form:

$$\begin{aligned} \frac{\partial u}{\partial t} + \frac{\partial uv}{\partial y} + \frac{\partial uw}{\partial z} - fv &= - fv_g - \frac{1}{\rho_0}\frac{\partial \tau_x}{\partial z} \,, \\ \frac{\partial v}{\partial t} + \frac{\partial v^2}{\partial y} + \frac{\partial vw}{\partial z} + fu &= fu_g - \frac{1}{\rho_0}\frac{\partial \tau_y}{\partial z} \,, \\ \frac{\partial b}{\partial t} + \frac{\partial bv}{\partial y} + \frac{\partial bw}{\partial z} &= -\frac{\partial G}{\partial z} \,, \end{aligned} \tag{2.2}$$

where

$$u_g = \frac{1}{f}\int_z^\infty \frac{\partial b}{\partial y}\,\mathrm{d}\bar{z} \,, \quad v_g = \frac{bS_x}{f} \,, \tag{2.3}$$

are the geostrophic velocities, τ_x and τ_y the turbulent fluxes of momentum, and G the turbulent buoyancy flux (lateral turbulent fluxes are ignored). The z-component of the velocity vector is denoted by w, computed from a continuity equation of the form:

$$\frac{\partial v}{\partial y} + \frac{\partial w}{\partial z} = 0 \quad . \tag{2.4}$$

For the idealized flows discussed in the following, it is assumed that $u, v, b \to 0$ for $z \to \infty$, i.e. far above the interface of the gravity current.

The differential equations in (2.2)-(2.4) form the basis for the analysis of gravity currents in this work. Identical equations have been used in the modeling study in Paper 5 by Umlauf et al. (2010), and different types of simplifications are discussed in Papers 1-4. More specifically, in Paper 1, Arneborg et al. (2007) considered a combined model-data approach with the help of a one-dimensional (vertical) set of equations derived from (2.2)-(2.4) by assuming that cross-channel derivatives can ignored, implying through (2.4) that all advection terms vanish. In the theory of Umlauf and Arneborg (2009b) (Paper 4), cross-channel gradients were retained but the flow was assumed to be quasi-stationary, which turned out to be sufficient to explain the complex lateral density structure in these flows.

2.2.2 Representation of the turbulent fluxes

While for the observational data described in Papers 1-4, the turbulent fluxes appearing on the right hand side of (2.2) have been estimated from different types of turbulence measurements, for the numerical solutions described in Paper 1 by Arneborg et al. (2007) and Paper 5 by Umlauf et al. (2010) a turbulence closure model was required. A detailed account of this rather complex issue is given in the review article by Umlauf and Burchard (2005), which includes the description of the turbulence models used in Papers 1 and 5.

Briefly, in these turbulence models the turbulent fluxes of momentum, τ_x and τ_y, and the buoyancy flux G are computed from gradient expressions of the form:

$$\frac{\tau_x}{\rho_0} = -\nu_t \frac{\partial u}{\partial z} \,, \quad \frac{\tau_y}{\rho_0} = -\nu_t \frac{\partial v}{\partial z} \,, \quad G = -\nu_t^b \frac{\partial b}{\partial z} \,, \tag{2.5}$$

where the turbulent diffusivities,

$$\nu_t = c_\mu \frac{k^2}{\varepsilon} \ , \quad \nu_t^b = c_\mu^b \frac{k^2}{\varepsilon} \ , \tag{2.6}$$

follow from an algebraic second-moment turbulence model combined with two prognostic transport equations for the turbulent kinetic energy k and the dissipation rate ε (or, as in Arneborg et al. (2007), for the specific dissipation rate $\omega = \varepsilon/k$). The functions c_μ and c_μ^b depend on the non-dimensional stability parameters Sk/ε and Nk/ε, where S is the total vertical shear and $N^2 \equiv \partial b/\partial z$ defines the buoyancy frequency N. Numerical and implementation issues are discussed in the documentation of the General Ocean Turbulence Model (GOTM, see Umlauf et al., 2005).

A particular problem in the description of gravity currents with numerical models is related to the fact that, at least in non-rotating flows, the vertical shear and thus the shear production of turbulent kinetic energy vanishes at the velocity maximum. A number of frequently used turbulence models that relate the turbulent diffusivity to the gradient Richardson number, $Ri = N^2/S^2$, will fail to predict mixing correctly at such locations where $Ri \to \infty$. A similar problem appears at the velocity maximum of jet-like oceanic currents like the equatorial undercurrent, suggesting that this effect is of some general relevance. Special modeling strategies required to overcome these turbulence modeling issues are discussed by Umlauf (2009), included in this thesis as Paper 7.

2.3 Bulk dynamics

Much of the progress made in recent years with the theoretical description of frictionally controlled gravity currents was based on vertically integrated reduced-gravity models, which for this reason are briefly reviewed here. The key assumption in this approach is that the gravity current can be represented as a homogeneous material volume of fluid with constant (negative) buoyancy b, superimposed by an infinitely thick stagnant layer with $b = 0$. This type of approximation, sometimes referred as the 1.5-layer model, applies in situations where the entrainment stress at the interface is dynamically insignificant, and the time scales considered are small compared to the time scale for significant changes of the interior buoyancy due to mixing with ambient water (Wåhlin, 2004; Darelius and Wåhlin, 2007). While a number of interesting results can be obtained with this simplified system, the main purpose of this chapter is to demonstrate that rotational effects distort the interfacial density structure to an extent that is not any more consistent with the geometric assumptions of the 1.5-layer model.

2.3.1 Governing equations

The geometry of the 1.5-layer model is illustrated in Figure 2.2 for a gravity current passing through an infinitely long channel (the case of a gravity current passing along an infinitely long submarine ridge is completely analogous). The flow consists of a buoyancy-driven near-bottom layer of thickness H, bounded from above by a material free surface representing the density interface at $z = \eta$, and from below by topography ($z = -D$) such that $H = \eta + D$ (Figure 2.2).

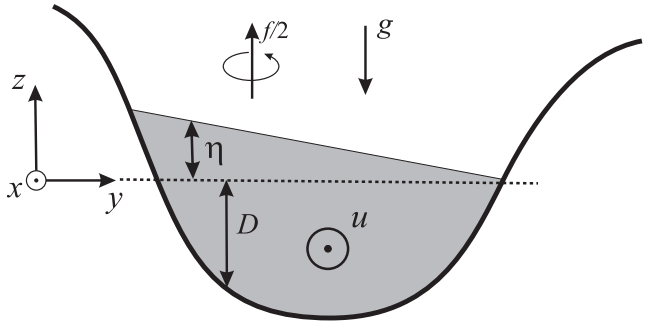

Figure 2.2: Geometry of the 1.5-layer model for a rotating gravity current passing through an infinitely long channel. Note that the coordinate system is titled in the down-channel direction as shown in Figure 2.1.

Using the standard kinematic boundary conditions for a material free surface, and the additional assumption that u and v are vertically constant, (2.4) may be integrated to yield an equation for the interface elevation:

$$\frac{\partial \eta}{\partial t} = -\frac{\partial vH}{\partial y} \quad . \tag{2.7}$$

Analogously, it can be shown that integration of (2.2) results in an integrated momentum budget of the form

$$\begin{aligned} \frac{\partial uH}{\partial t} + \frac{\partial uvH}{\partial y} - fvH &= -bHS_x - C_D\,|\boldsymbol{u}|\,u\,, \\ \frac{\partial vH}{\partial t} + \frac{\partial v^2H}{\partial y} + fuH &= bH\frac{\partial \eta}{\partial y} - C_D\,|\boldsymbol{u}|\,v\,, \end{aligned} \tag{2.8}$$

where the bottom stress has been expressed by a quadratic drag law with C_D denoting the drag coefficient, and $|\boldsymbol{u}| = (u^2 + v^2)^{1/2}$ the total speed. Wåhlin (2002) has compared this drag law to different alternatives, including a linear representation of bottom drag and a parametrized Ekman layer, finding, however, only small differences among these models if the corresponding drag coefficients are adjusted to yield comparable Ekman layer thicknesses. Although complicating the analytical solution (2.8), the quadratic relationship

is preferred here because it can be shown to be consistent with classical turbulent boundary-layer scaling and with the representation of near-bottom turbulence in the turbulence models employed in Papers 1, 5, 6, and 7. A quadratic dependency with a drag coefficient of the order of $C_D = 10^{-3}$ was also inferred from the direct bottom stress measurements discussed in Paper 3 (Umlauf and Arneborg, 2009a).

Finally, it should be noted that no new information is obtained from the integrated buoyancy equation in (2.2): in the absence of entrainment the buoyancy b remains constant and homogeneous for all times.

2.3.2 Properties of the solution

The expressions in (2.7) and (2.8) form a closed set of equations for the 3 unknowns u, v, and η. To illustrate the properties of this system, it is numerically solved here with the help of a conservative finite volume approach, using resolutions in space and time that are high enough to insure fully converged results. These simulations are not part of Papers 1-5, and mainly serve the purpose of introducing the basic principles and consequences of frictional control.

The gravity currents described in Papers 1-5 exhibit a typical thickness of the order of 10 m, and, laterally constrained by the local channel topography, a width of the order of 10 km. The basic properties of these flows will be illustrated with the help of an idealized geometry, consisting of an infinitely long, cosine-shaped channel with down-channel slope $S_x = 5 \times 10^{-4}$, and bottom drag coefficient $C_D = 10^{-3}$. The simulations are initialized with zero velocities, a flat interface, a buoyancy contrast of $b = -0.1$ m s^{-2}, and a local thickness of $H = 10$ m at the deepest point of the channel, resulting in a width of 10 km at the interface level. The local latitude of 55°N corresponds to a Coriolis parameter of $f = 1.12 \times 10^{-4}$ s^{-1}, and a local inertial period of $T_f = 14.65$ h. These values are consistent with the observations described in Papers 2, 3 and 4 (Umlauf et al., 2007; Umlauf and Arneborg, 2009a,b), and the vertically resolved simulations in Paper 5 (Umlauf et al., 2010), which facilitates a direct comparison.

Temporal evolution

Snapshots of the lateral structure of the solution at selected times (Figure 2.3) show the evolution of a swift down-channel flow with speeds reaching 0.7 m s^{-1}, and clear indications for a geostrophic adjustment of the interface. Near the edges, the down-channel speeds become vanishingly small due to the increasing influence of friction, and the geostrophically balanced interface slope tends to zero. A similar behavior was already pointed out by Wåhlin (2002, 2004), who considered the stationary case with linear friction. Time series

of the velocities and interface displacements in the channel center (Figure 2.4) reveal that already after one inertial period the gravity current has reached approximately stationary conditions. Oscillations in the cross-channel speed and interface elevation, easily identified as cross-channel internal seiches with a period of approximately 6 h, are quickly damped out due to bottom friction (Figure 2.4b,c). This unexpectedly strong damping can be understood by comparing the gravity current solution with the non-rotating, purely two-dimensional cross-channel seiching problem with vanishing down-channel flow ($u = 0$). For the pure seiching case, the drag term on the right hand side of (2.8) adopts the form $C_D\,|v|\,v$, whereas for the channelized gravity current considered here ($u \gg v$) one finds $C_D\,|\boldsymbol{u}|\,v \approx C_D uv$. This is a factor of $u/v \gg 1$ larger compared to the seiching case, demonstrating that the swift down-channel flow is essential for the strong damping and quick geostrophic adjustment.

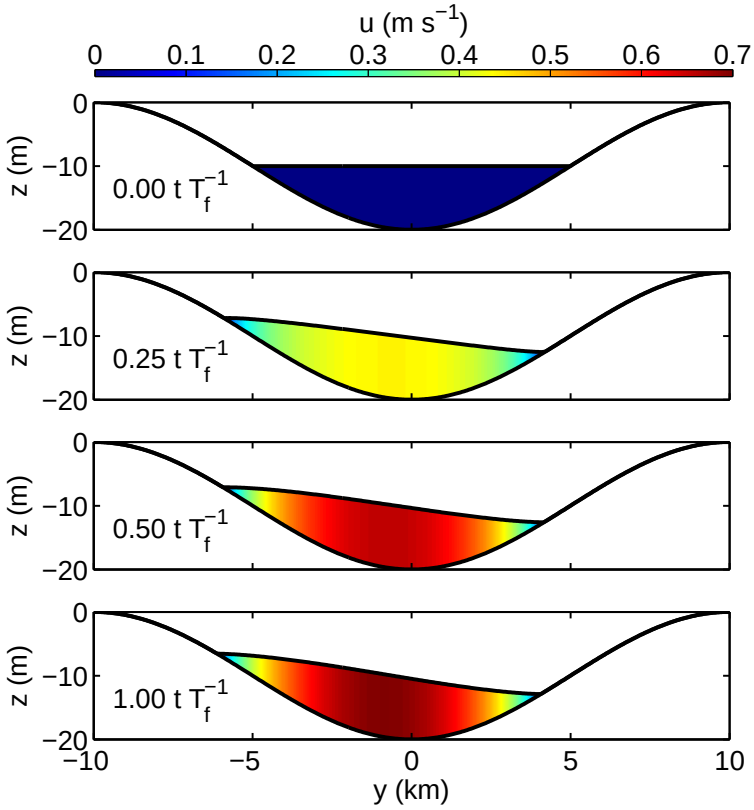

Figure 2.3: Numerical solution of (2.7) and (2.8) at different times (here specified as fractions of the inertial frequency $T_f = 14.65$ h). Model parameters are: $S_x = 5 \times 10^{-4}$, $b = -0.1$ m s^{-2}, $C_D = 10^{-3}$, and $f = 1.12 \times 10^{-4}$ s^{-1}.

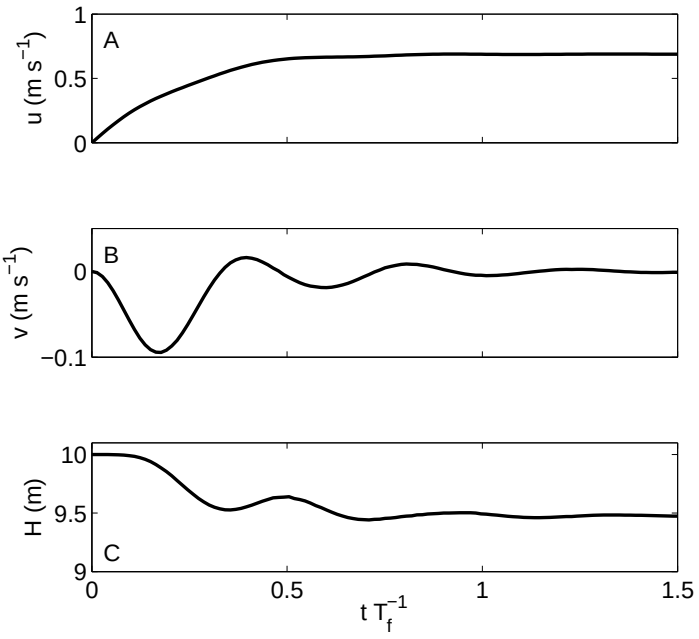

Figure 2.4: Solutions of (2.7) and (2.8) for (a) the down-channel velocity, (b) the cross-channel velocity, and (c) the total thickness of the gravity current, all evaluated in the center of the channel. Parameters correspond to those given in Figure 2.3.

Stationary solution

Given the quick adjustment time of the simulated flow, it is interesting to look for stationary solutions of (2.7) and (2.8). In this case, all rate terms vanish by definition, and the continuity equation (2.7) requires $v = 0$ everywhere. Thus, without further assumptions, (2.8) can be written as

$$\begin{aligned} bHS_x &= -C_D\, u^2 \,, \\ fu &= b\frac{\partial \eta}{\partial y} \,, \end{aligned} \tag{2.9}$$

which reveals the essential dynamical components of a rotating, frictionally-controlled gravity current: (a) a balance between bottom friction and the down-channel interfacial pressure gradient, and (b) a simple geostrophic balance in the cross-channel direction.

Further insight into the physical properties of (2.9) can be gained by re-formulating it in non-dimensional form. To this end, it is helpful to introduce the Ekman number,

$$E_k = \frac{C_D u}{fH} \,, \tag{2.10}$$

measuring the ratio of the bottom stress, $C_D u^2$, and the Coriolis force, fuH. With the help

(2.9), the Ekman number can be expressed in two alternative non-dimensional ways that reveal some interesting properties:

$$E_k = -\frac{S_x}{\eta'} = \left(\frac{\delta}{H}\right)^{\frac{1}{2}} , \tag{2.11}$$

where the prime denotes the cross-channel derivative with respect to y, and

$$\delta = -\frac{bC_D S_x}{f^2} \tag{2.12}$$

is a fixed length scale that combines all parameters of the problem. The first equality in (2.11) shows that the Ekman number can be interpreted as the ratio of the down-channel and cross-channel interface tilts: flows with larger Ekman number, and thus greater relative importance of frictional effects, exhibit a larger relative down-channel tilt. The last term in (2.11) suggests that δ has the physical significance of an Ekman layer thickness. From inspection of the shape of this term in (2.12), it is easily seen that slowly rotating flows in steep channels with large bottom roughness and large buoyancy contrast exhibit a stronger relative importance of frictional effects.

Since the topography D is given, and $\eta' = H' - D'$ (see Figure 2.2), the second equality in (2.11) can also be understood as a first-order differential equation for the plume thickness $H(y)$. In spite of its apparent simplicity, the non-linearity of (2.11) makes it rather difficult to find closed analytical solutions except for very simple topographic shapes. A numerical solution of (2.11), however, is easily found, and shown in Figure 2.5 for the parameter set used above. The interface elevation is seen to be almost identical to that shown in Figure 2.3 after one inertial period, confirming the above conclusion that at this time the solution is already close to the steady state.

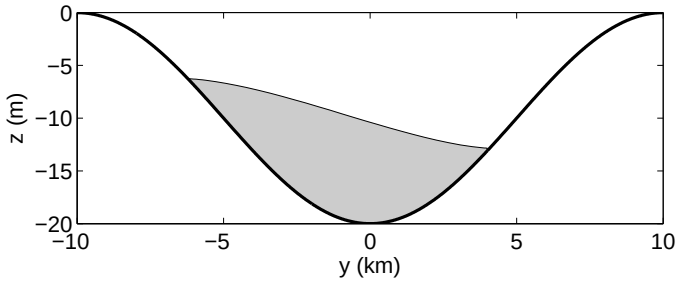

Figure 2.5: Numerical solution of (2.11) for the parameters also used in Figure 2.3 above.

2.4 Observations

The observational program described in Papers 1-4 focused on a submarine channel in the Western Baltic Sea that was found to be the major pathway for saline bottom gravity

currents entering through the Sound from the Kattegat (Figure 2.6). Measurements included moored current meters in the center of the channel, ship-based measurements with vessel-mounted and towed ADCPs, as well as densely-spaced turbulence microstructure profiling. The latter was performed with a free-falling instrument providing nearly full-depth profiles of temperature, conductivity, and current shear at centimeter scales, from which the most important hydrographic and turbulence parameters (density, dissipation rate, turbulent diffusivity, etc.) can be derived. Technical aspects of these measurements are described in Paper 1 (Arneborg et al., 2007) and Paper 3 (Umlauf and Arneborg, 2009a).

Data of this type were obtained during different years with high resolution in time (e.g., a few minutes per microstructure profile) at a location in the center of the channel (Paper 1 by Arneborg et al., 2007), as well as on different transects across the channel (Papers 2-4 by Umlauf et al., 2007; Umlauf and Arneborg, 2009a,b). On one of these transects (Figure 2.6c), data from two simultaneously operating ships provided a synoptic and highly-resolved view of the cross-channel structure of a vigorously turbulent bottom gravity current that, regarding both resolution and parameter range, can still be considered unique. This detailed data set has provided a number of new insights into the internal structure and dynamics of turbulent rotating gravity currents that will be described in the following.

2.4.1 Non-dimensional bulk parameters

A frequently used parameter for the characterization of gravity currents is the Froude number, here defined as

$$Fr = \frac{\Delta U}{(-BH)^{\frac{1}{2}}} , \tag{2.13}$$

where ΔU and B denote suitably defined bulk velocity and buoyancy differences between the gravity current and the ambient fluid. In Paper 4, Umlauf and Arneborg (2009b) have shown that in the center of the channel this parameter is typically in the range $0.2 \leq Fr < 0.5$, similar to $Fr \approx 0.5$ found in Paper 1 at the same location during a previous campaign. These Froude numbers are substantially below the critical value $Fr = 1$, indicating that hydraulic control and interfacial entrainment are not expected to have significant dynamical effects (Turner, 1986; Cenedese and Adduce, 2010).

A second important parameter is the Ekman number that was already introduced in (2.10) in the context of the 1.5-layer model with parametrized bottom friction. Here, it is reformulated somewhat more generally as

$$E_k = \frac{|\boldsymbol{\tau}_b|}{\rho_0 f U H} , \tag{2.14}$$

where $\boldsymbol{\tau}_b$ denotes the bottom stress vector, and U a typical bulk speed, equal to ΔU only if the fluid above the gravity current is stagnant. During different campaigns analyzed

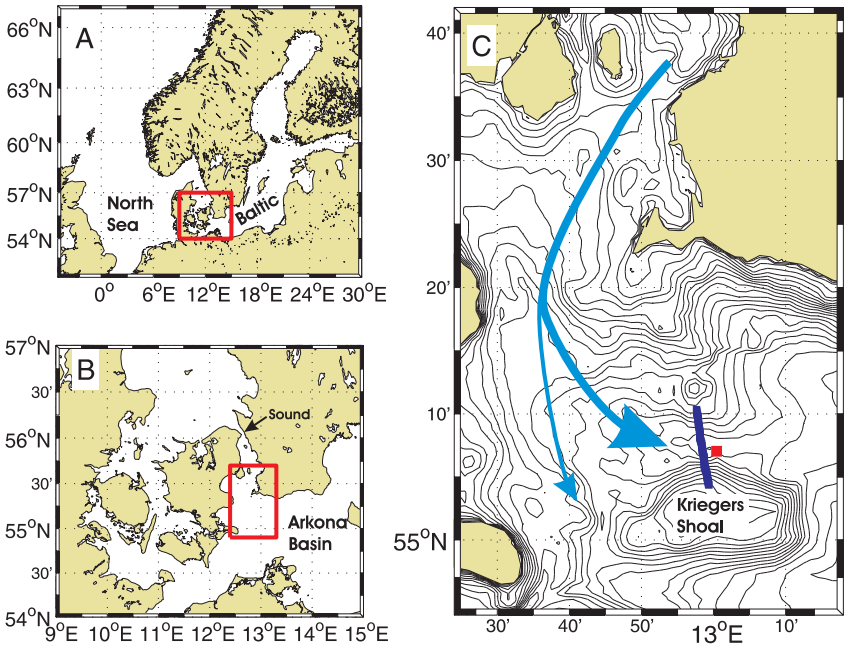

Figure 2.6: Maps of (a) North Sea and Baltic Sea, (b) Western Baltic Sea, and (c) study area in the Arkona Basin. The position of the moored ADCP and ADV is marked by the red rectangle, and the approximately 11 km long cross-channel transect north of Kriegers Shoal is indicated by the blue line. Ship-based observations on the transect included densely-spaced turbulence microstructure and ADCP measurements. The pathways of saline near-bottom currents entering through the Sound are schematically indicated by the blue arrows. Depth contours are given at 2-m intervals.

in paper 1 and 4 (Arneborg et al., 2007; Umlauf and Arneborg, 2009b), Ekman numbers of the order of 1 were found, underlining the first-order importance of frictional effects in the gravity currents studied here. In view of these findings, it may thus be expected that frictional rather than hydraulic effects constitute the essential control mechanism.

2.4.2 Cross-channel structure

A combined view of the cross-channel density and velocity structure, adapted from Paper 3 (Umlauf and Arneborg, 2009a), is shown in Figure 2.7. This figure reveals a dense bottom layer of up to 15 m thickness, separated from the ambient fluid by a well-defined interface. The density anomaly of the gravity current exhibits some variability but is of the order of 10 kg m^{-3}, and therefore about one order of magnitude larger compared to typical large-scale overflows in the ocean (e.g., Baringer and Price, 1997a; Seim and Fer, 2011). The clear signal in density is mirrored in the velocity distribution, showing a compact layer of fluid

moving with speeds up to 0.7 m s^{-1} towards East, down the channel. Associated with this swift flow is a lateral interface tilt that Umlauf and Arneborg (2009b) showed to be largely geostrophically balanced.

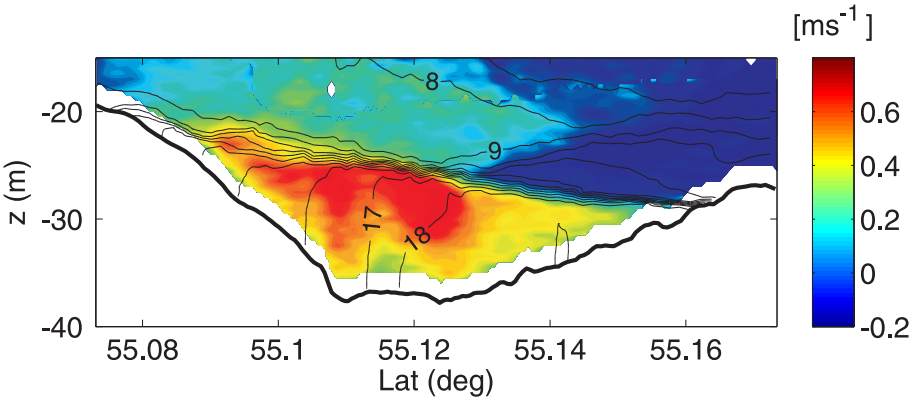

Figure 2.7: Transverse view of down-channel velocity and density (ρ−1000 kg m^{-3}) structure along the cross-channel transect marked in Figure 2.6c. Data were collected within less than 3 hours on 17 November 2005. Modified figure from Umlauf and Arneborg (2009a).

A closer look into the density structure shown in Figure 2.7 reveals two remarkable features that cannot be explained in the framework of the 1.5-layer model but will be central for the following analysis. First, it is evident that the interface, rather than representing a sharp density jump, has the character of a wedge-shaped transition region with strongly varying thickness, gradually increasing from less than a meter on the northern rim of the channel up to several meters on the opposite side. The second interesting feature is the evolution of a lateral density gradient in the interior region below the interface in the southern part of the channel, where nearly vertical isopyncals are observed (the northern part is not affected by this). This rather peculiar density structure seems to be a robust feature, observed during different years at the same location, as well as in other gravity currents in the Baltic Sea, e.g. in the Bornholm Channel in the Southern Baltic (Petrén and Walin, 1976; Reissmann et al., 2009) and in the Stolpe Channel in the Baltic Proper (Paka et al., 1998; Zhurbas et al., 2012). The dynamical reasons for these observed patterns are tightly connected to the transverse circulation that will be discussed in the following.

2.4.3 Secondary circulation

The unexpected complexity of the lateral density structure is also mirrored in the velocity timeseries derived from the ADCP moored near the center of the channel (Figure 2.8). While the signal of the down-channel component merely confirms the stationarity of the flow, and the vertical structure already found in Figure 2.7, the transverse component reveals a surprisingly complex and stable pattern. A three-layer circulation can be distinguished,

with a pronounced jet-like current (to the left, looking upstream) inside the interface, a return flow in the interior just below the interface, and a current reversal in the lower part of the flow. Similar observations had already been made in Paper 1 by Arneborg et al. (2007), who were puzzled by the fact that the near-bottom flow was exactly opposite to that predicted from Ekman theory. A full cross-channel transect of the transverse velocity discussed in Paper 3 by Umlauf and Arneborg (2009a) has shown that the interfacial jet persists, with variable strength, across the whole width of the gravity current, whereas the near-bottom layer with the current reversal is confined to a relatively narrow region in the center of the channel (not shown). A dynamical explanation for these features was given in Papers 4 and 5 as discussed in more detail below.

Note that, consistent with the strong damping suggested by the model results displayed in Figure 2.4, no significant cross-channel internal seiching motions are observed. This indicates that the observations of the transverse structure discussed above have been synoptic, which is rarely the case in oceanic gravity current studies that generally suffer from undersampling due to the strong variability induced by tides and flow instabiltities.

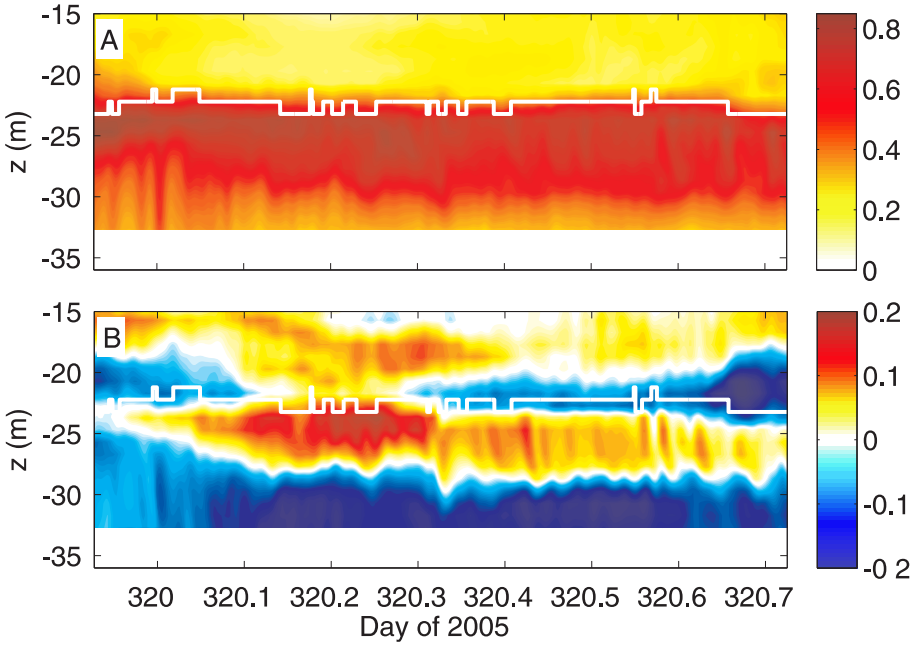

Figure 2.8: Time series of (a) down-channel velocity, and (b) cross-channel velocity (positive north) near the channel center (position is marked in Figure 2.6c). The white line marks the interface layer, here defined as the ADCP bin with maximum vertical shear. The time period includes the measurements shown in Figure 2.7, the latter corresponding to 2.7 hours during days 320.33-320.44. Modified figure from Umlauf and Arneborg (2009a).

2.4.4 Mixing and entrainment

The rate at which ambient fluid is entrained by turbulent motions into a dense bottom current determines its density and final interleaving depth, and is therefore of primary interest in the investigation of such flows. Of similar relevance is the effect of turbulence on the bottom and interfacial stresses that both may be essential for the bulk dynamics. The standard approach for quantifying these processes has been based on the construction of budgets at different downstream cross-sections of the gravity current (e.g., Baringer and Price, 1997a,b), which, however, involves some rather serious model assumptions (e.g., stationarity), and generally leads to large uncertainties if entrainment rates are small. In such cases (the gravity currents in the Baltic Sea form one example), direct observation of the turbulent fluxes is often the only available alternative for obtaining reliable entrainment estimates.

However, the technical and logistical challenges involved in direct turbulence measurements have so far prevented their wide-spread use in oceanic gravity current studies. Shear-microstructure measurements, the most involved but also most generally applicable and accurate technique of this type, have been used to obtain mixing parameters only in a few examples, among them two campaigns in the Mediterranean outflow (Wesson and Gregg, 1994; Johnson et al., 1994a), an investigation of the Storfjorden overflow (Fer, 2006), and a recent study of mixing in the Faroe Bank Channel overflow (Fer et al., 2010; Seim and Fer, 2011). Following a different method, a few studies have also attempted to estimate mixing parameters from the statistical analysis of density overturns in CTD profiles, which, by energetic arguments, can be related to energy dissipation and mixing (Fer et al., 2004; Mauritzen et al., 2005; Peters and Johns, 2005). Except for the data discussed in this work, the only direct measurements of the bottom momentum flux (or stress) in a gravity current appear to be the observations in the Red Sea outflow plume by Peters and Johns (2006).

While providing valuable insights into the mixing behavior of gravity currents that would have been unattainable with any other means, these studies were generally not able to provide a synoptic and spatially coherent picture of mixing and entrainment due to the large spatial scales, large depth, and strong temporal variability in the presence of tides and flow instabilities. Because of the absence of tides and the stabilizing effects of topography and friction, gravity currents in the Baltic Sea exhibit a much smaller temporal variability than their large-scale counterparts in the ocean, and are much more easily accessible with turbulence instrumentation. Yet, their spatial scales are large enough to make rotation a first-order effect, and to guarantee that molecular (viscous) effects can be ignored. For these reasons, the Baltic Sea can be viewed as an ideal natural laboratory for studying the effects of turbulence and rotation in dense gravity currents.

These facts have been exploited in Paper 1 by Arneborg et al. (2007), who presented the

first highly resolved timeseries of simultaneous observations of vertical current shear, stratification, and turbulence dissipation rates in a real oceanic gravity current. Quite surprisingly, in view of the low Froude number mentioned above ($Fr \approx 0.5$) , these observations have revealed a vigorously turbulent flow with dissipation rates reaching values around $\varepsilon = 10^{-5}$ W kg^{-1} even in the strongly stratified interface region, which was 2–3 orders of magnitude above the ambient values. These data have turned out to fill an important gap for reliable entrainment estimates at low Froude numbers that are notoriously difficult to access in laboratory experiments due to viscous effects (Cenedese and Adduce, 2008). The importance of reliable data in this parameter range has been emphasized in a number of studies suggesting entrainment at low Froude numbers to be essential for the long-term propagation and late-stage evolution of large-scale oceanic overflows (Wåhlin and Cenedese, 2006; Hughes and Griffiths, 2006). With the help of data from the Baltic Sea, new entrainment laws, valid also in the low Froude number range, are now being developed (Cenedese and Adduce, 2010; Wells et al., 2010).

The single-point measurements in the center of the channel discussed in Paper 1 by Arneborg et al. (2007) were later extended to include full cross-channel transects. These new data, first presented in Paper 2 by Umlauf et al. (2007), combined densely-spaced turbulence microstructure measurements with the nearly full-depth velocity observations discussed above, providing the first complete, detailed, and synoptic view of the transverse structure of a rotating gravity current at very high Reynolds number. These observations (Figure 2.9) have shown that energy dissipation is characterized by spatially coherent regions that were attributed to different dynamical regimes: a frictional near bottom layer, a turbulent interface region, and a "quiet core" with very low dissipation rates, located in the vicinity of the velocity maximum, where shear production of turbulence is small. Similar observations were made in the Bornholm Channel, connecting the Arkona Basin with the neighboring Bornholm Basin (Reissmann et al., 2009). The relation between these observed mixing patterns and the internal dynamics of the flow was the focus of Papers 3-5 that are briefly summarized in the following.

2.5 Analysis

As a first step towards a physical interpretation of the observations discussed above, it is instructive to compare the velocity measurements in Figure 2.7 with the results from the idealized 1.5-layer model constructed in Section 2.3. With model parameters chosen to approximately correspond to those found from the analysis of field data, and after stationary conditions have been reached (last panel in Figure 2.3), the model is seen to yield an acceptable representation of the most important bulk characteristics, like interface tilt, maximum speed, and lateral velocity structure. This shows that already the most basic

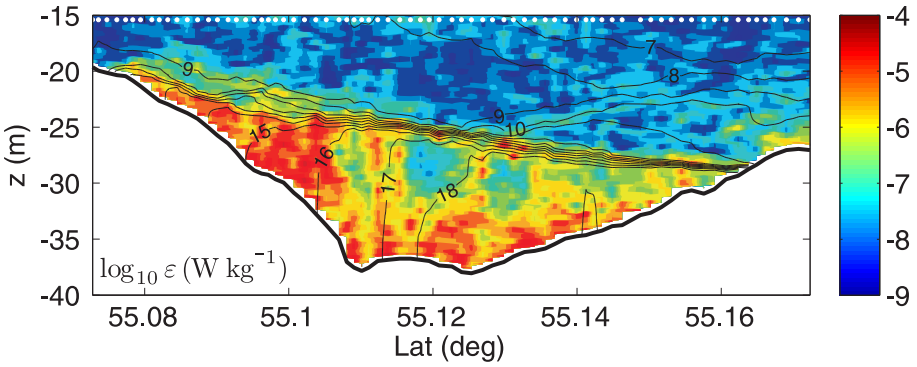

Figure 2.9: Same as Figure 2.7 but now the turbulent dissipation rate is shown. White dots at the top indicate the positions of 74 microstructure casts used for this analysis. These observations have been performed simultaneously with the velocity measurements from combined vessel-mounted and towed ADCPs displayed in Figure 2.7. Figure replotted from data published in Umlauf et al. (2007).

mathematical representation of frictional control according to (2.9) is able to capture the essential physics of the problem, implying that the memory of upstream conditions, a central component of hydraulic models that is ignored here, cannot be an important factor. This finding also holds for the more advanced modeling study in Paper 5 by Umlauf et al. (2010), described below, which may be viewed as an a-posteriori justification for ignoring upstream gradients in the derivation of the momentum budget in (2.2).

In spite of the fact that the 1.5-layer model yields an acceptable first-order description of the bulk dynamics of the flow, models of this type cannot, by definition, provide an explanation for the internal density and velocity structure. The investigation of the reasons for and dynamical implications of these features was the central topic of Papers 1-5. The most significant results will be summarized in the following, starting with the development of a conceptual picture for the secondary circulation.

2.5.1 Cross-channel dynamics

An insightful interpretation of (2.9) that has motivated much of the work discussed below was given by Wåhlin (2002, 2004), who pointed out that the down-channel component in (2.9) may be written as:

$$vH = v_g H + v_f H \equiv 0 \,, \tag{2.15}$$

where

$$v_g H = \frac{bS_x}{f} H \,, \quad v_f H = \frac{C_D}{f} u^2 \quad . \tag{2.16}$$

These relations state that the net transverse transport can be viewed as consisting of two opposing components that exactly cancel under stationary conditions: a negative component, $v_g H$, geostrophically balancing the down-channel interface tilt, and a positive component, $v_f H$, representing the cross-channel Ekman transport associated with the down-channel bottom drag. This provides the perhaps clearest illustration of the importance of frictional effects for the downward transport of fluid that would otherwise propagate along topography as a geostrophically balanced flow (Wåhlin, 2002).

The corresponding relation for the more general problem with vertically varying velocities can be derived from the down-channel component of (2.2), re-arranged in the form:

$$v = v_g + v_f + \frac{1}{f}\frac{\mathrm{D}u}{\mathrm{D}t}\,, \tag{2.17}$$

where v_g denotes the geostrophically balanced cross-channel velocity defined in (2.3), $\mathrm{D}/\mathrm{D}t$ the material derivative, and

$$v_f = \frac{1}{\rho_0 f}\frac{\partial \tau_x}{\partial z} \tag{2.18}$$

the frictionally-induced transverse velocity component (Umlauf et al., 2010).

Considering first the stationary, non-entraining 1.5-layer system depicted in Figure 2.2, but now allowing for vertically variable velocities, the continuity equation in (2.7) still implies that the vertical integral of v vanishes. The same, however, does not apply for the *local* contributions of the terms on the right hand side of (2.17), which leads to the important conclusion that a transverse secondary circulation forms an essential component of the down-channel momentum budget. Some information about the vertical structure of this secondary flow can be obtained by focusing on the expected vertical variability of v_g and v_f, respectively. The former remains vertically constant in the unstratified region below the interface, whereas the latter is likely to exhibit a near-bottom intensification due to the increasing importance of frictional effects. Considering the stationary linearized problem, the last term in (2.17) vanishes, and is otherwise very small as suggested by the non-linear simulations of Umlauf et al. (2010). Equation (2.17) therefore suggests a two-layer secondary circulation with a near-bottom flow to the right (looking upstream) according to Ekman theory, and a return flow in the upper part of the gravity current (Figure 2.10a). It is important to note, however, that the near-bottom flow is usually much smaller than the pure Ekman transport due to the compensating effect of v_g, which is often overlooked (Johnson and Sanford, 1992; Paka et al., 1998). Moreover, if the plume thickness is small compared to the bottom Ekman layer thickness (this is the case for the shallow gravity currents studied in this work), v_f will not change appreciably in the vertical, and is therefore compensated nearly everywhere by the constant v_g. Under these conditions, the secondary circulation is expected to be small.

The situation is further complicated by the fact that, contrary to the simple 1.5-layer model assumed above, real oceanic gravity currents often exhibit a rich internal density structure,

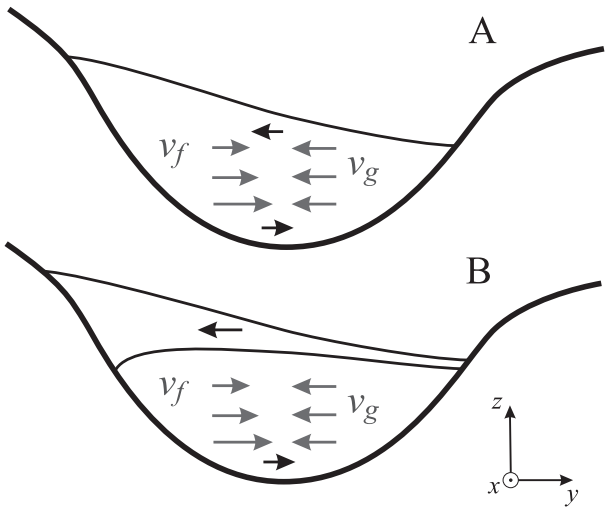

Figure 2.10: Schematic view of different components (gray arrows) of the secondary circulation for the two cases with (a) an idealized 1.5-layer flow, and (b) a realistic interface with finite thickness (upper and lower edges of the interface are indicated as thin black lines). Black arrows illustrate the residual flow. The main (down-channel) flow is out of the page.

including an interface layer that may cover a significant fraction of the total thickness (e.g., Peters et al., 2005; Umlauf et al., 2007; Fer et al., 2010). According to (2.17), the presence of internal stratification is likely to impact on the secondary circulation in at least the following ways: (a) by creating additional baroclinic pressure gradients that modify v_g; (b) by suppressing turbulence which affects the secondary circulation via v_f; and (c) by the appearance of dynamically relevant "entrainment stresses" due to mixing in the interface region, which is represented by the last term in (2.17) as shown by Umlauf et al. (2010). On the other hand, however, any modification of the secondary circulation due to these effects will influence stratification by lateral advection of density, thus creating a complex feedback mechanism between stratification and lateral circulation.

The interplay of these different mechanisms is schematically illustrated in Figure 2.10b, showing a gravity current with a stratified interface layer of variable thickness. Assuming that the internal stratification in the interior region, below the interface, is negligible, the secondary circulation in this region is expected to be similar to that described for the 1.5-layer model above. The more complicated interface region can be understood by considering the one-dimensional version of (2.17), i.e. by ignoring lateral advection:

$$v(z,t) = v_g(z,t) + v_f(z,t) + v_E(z,t) \ , \tag{2.19}$$

where $v_E = f^{-1}\,\partial u/\partial t$ has been introduced for convenience.

Inside the stably stratified interface, the buoyancy b will decrease from $b = 0$ at the top of the interface to its minimum value at the lower edge. According to (2.3), we therefore expect

$v_g < 0$ inside the interface, corresponding to a geostrophically balanced flow to the left (looking upstream), increasing in magnitude with depth. The size and even the sign of the frictional component v_f is more difficult to estimate due to its dependency on the turbulent momentum flux τ_x. Near the upper edge of the interface, however, the stress is likely to decrease from some value $\tau_x > 0$, required to accelerate freshly entrained fluid, towards zero at the top of the interface. According to (2.18), this implies $v_f < 0$, such that v_f and v_g will point into the same direction in the uppermost part of the interface. Most important in this context is the fact that the vertical integral of (2.18) corresponds exactly to the bottom Ekman transport, $\tau_x^b/(\rho_0 f)$, which implies that v_f does not provide any net transport inside the interface. It can therefore not be associated with any bulk interface deformation due to lateral flow divergence, as sometime erroneously assumed. This is different for the last term, v_E, which involves the acceleration of newly entrained fluid, and does not integrate to zero. This acceleration is positive (down-channel) in the interface region, thus leading to a positive contribution ($v_E > 0$) to the interfacial transport that opposes the geostrophically balanced component v_g. The vertical integral of v_E across the interface region can thus be interpreted as the net interfacial Ekman transport associated with the entrainment stress (see Paper 5 by Umlauf et al., 2010).

Therefore, as pointed out in Papers 4 and 5, if entrainment is small, the net transverse transport inside the interface will be dominated by v_g, pointing to the left (looking upstream) as illustrated in Figure 2.10b. This was shown to explain the observed interfacial jet as well as the wedge-shaped interface structure, the latter simply being a result of transport divergence and convergence, respectively, near the channel walls. Further complications arise if the interior region below the interface is stratified, leading to additional pressure gradients that modify v_g. This case will be discussed below.

2.5.2 Interpretation of observations and model results

Interfacial jet

First observational support for conceptual picture outlined above came from the single-point observations in the center of the channel discussed in Paper 1 by Arneborg et al. (2007). These authors were able to identify the interfacial jet in their data, as well as in a one-dimensional numerical model aimed at reproducing the vertical structure of the flow. At this early stage of the investigations, however, no satisfying dynamical explanation for this phenomenon could be provided. Nevertheless, Arneborg et al. (2007) recognized frictional effects as an essential component of the secondary circulation, and suggested a new entrainment law that, in addition to the traditionally used Froude number (e.g., Cenedese and Adduce, 2010), included also a dependency on the Ekman number E_k defined in (2.14). This aspect of the problem was investigated in more detail in Paper 4 by Umlauf

and Arneborg (2009b), who were able to establish a direct link between bottom friction, rotation, and the strength of the interfacial jet. As one of their key results, these authors were able to show that for $E_k > 1$ the transverse jet, rather than the down-channel flow, dominates the vertical shear inside the interface, thus explicitly illustrating the importance of Ekman number effects for entrainment in rotating gravity currents.

This was later confirmed in Paper 5 by Umlauf et al. (2010), who used a numerical model to show that shear-production of turbulence inside the interface is strongly affected by the presence of the jet. The model was based on the full set of equations in (2.2), numerically solved for a cosine-shaped channel topography with scales and parameters approximately corresponding to those described in the observational Papers 2–4. A full description of the model can be found in documentation of the General Estuarine Transport Model (GETM) by Burchard and Bolding (2002), except for the recently developed vertically adaptive numerical grid that is described in Hofmeister et al. (2010). As mentioned in Section 2.2, the turbulent fluxes were computed from a second-moment turbulence model described and analyzed in detail in Papers 6 and 7 (Umlauf and Burchard, 2005; Umlauf, 2009). Comparison of the computed dissipation rates and turbulent fluxes with the observed turbulence parameters has shown that the model yields an excellent representation of turbulent mixing (Umlauf et al., 2010).

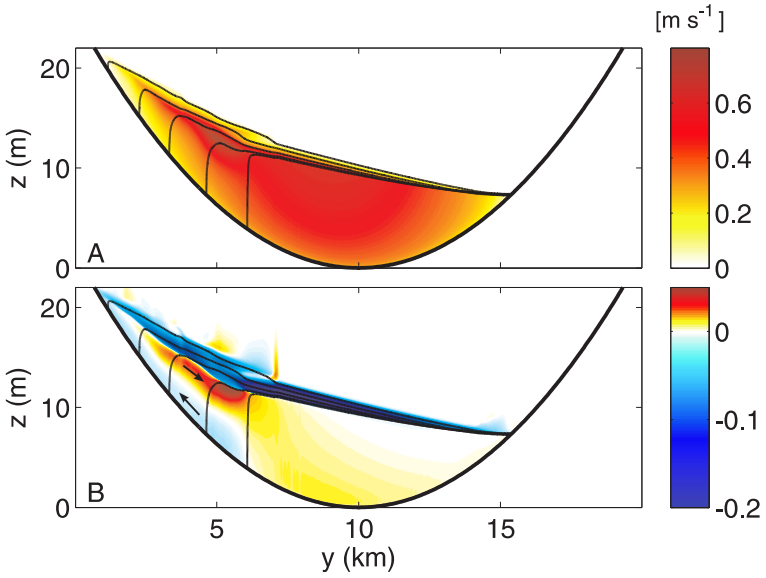

Figure 2.11: (a) Down-channel and (b) cross-channel velocity from the idealized two-dimensional numerical simulation by Umlauf et al. (2010). Simulations started from initial conditions with zero velocities and zero cross-channel interface slope. Results shown here correspond to the situation after two inertial periods, when cross-channel seiching motions have decayed. Black arrows in (b) indicate the direction of the secondary circulation. Modified figure from Umlauf et al. (2010).

The internal structure of velocity and density from these idealized simulations is displayed in Figure 2.11. Comparison with the vertically integrated simulations (see last panel in Figure 2.3) shows that both models predict comparable maximum down-channel velocities, a comparable reduction towards the edges, and similar lateral interface tilts, indicating that the bulk dynamics is represented in a similar way. Beyond this, however, the simulations in Paper 5 revealed a number of characteristic features that only the vertically resolved model was able to capture. Among them are the evolution of a wedge-shaped interface, the generation of lateral density gradients in the interior region below the interface, and the interfacial jet visible in Figure 2.11b. All of these modeled features are in close agreement with the observations (see Section 2.4), underlining the fact that the two-dimensional formulation of the problem in (2.2) provides a viable representation of the essential physics.

Motivated by this good agreement between model and data, Umlauf et al. (2010) used their simulations to investigate the dynamics and consequences of the secondary circulation in greater detail. To this end, they decomposed the transverse velocity into geostrophically balanced and frictional components according to (2.19) for a location in the center of the channel not affected by the lateral buoyancy gradients described above. Below the interface, the geostrophic and frictional components v_g and v_f were found to be of opposite sign but similar magnitude, therefore resulting only in a small net return flow (Figure 2.12). Approaching the interface from below, the frictional component v_f, however, decays more quickly than v_g, and even changes sign due to the increasing effect of the entrainment stress, such that a transverse circulation to the left (the jet) evolves. This dynamical behavior corresponds exactly to that anticipated in Section 2.5.1.

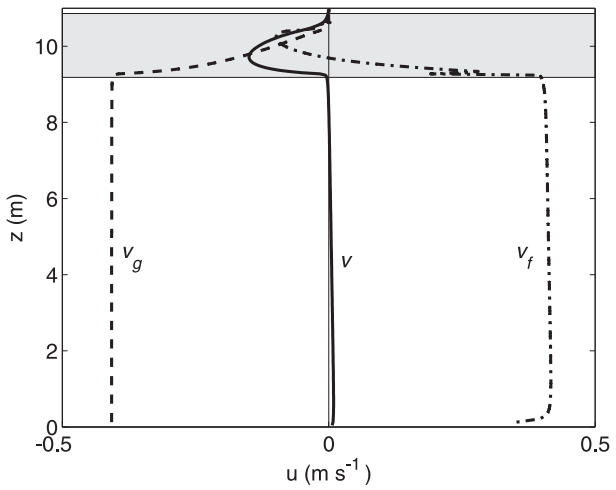

Figure 2.12: Modeled transverse velocity with components v_g and v_f from the idealized simulations by Umlauf et al. (2010). Lateral position corresponds to $y = 10$ km, exactly in the center of the channel shown in Figure 2.11. the gray-shaded area indicates the strongly stratified interface region. Figure adapted from Umlauf et al. (2010).

It is worth noting that similar wedge-shaped interfaces have also been found in observations of large-scale overflows (Johnson and Sanford, 1992; Mauritzen et al., 2005; Seim and Fer, 2011), as well as in laboratory investigations of rotating gravity currents (Johnson and Ohlsen, 1994; Davies et al., 2006; Darelius, 2008), and in numerical investigations (Kämpf, 2000; Ezer, 2006). Seeking for an explanation for the observed structure, previous investigations have either focused on hydraulic mechanisms (e.g., Hogg, 1983), or on the interplay between bottom and interfacial Ekman layers that was suspected to be responsible for the transverse circulation patterns observed in some of these flows (Johnson and Sanford, 1992; Johnson and Ohlsen, 1994; Paka et al., 1998; Ezer, 2006). All these previous studies, however, have failed to recognize the crucial role of the geostrophically balanced transverse velocity v_g.

Effect of lateral density gradients

An interesting phenomenon found in both observations (Figure 2.7) and model simulations (Figure 2.11) is the generation of a region with lateral density gradients associated with the presence of nearly vertical isopycnals in the interior of the gravity current below the interface. Similar patterns have also been found at other locations along the pathways of bottom gravity currents in the Baltic Sea, e.g. in the Bornholm Channel (Reissmann et al., 2009) and in the Stolpe Channel (Zhurbas et al., 2012), as well as in simulations of these flows with the help of high-resolution numerical models (Burchard et al., 2005, 2009; Hofmeister et al., 2010). This suggests a rather robust mechanism that warrants further study.

Already in Paper 1, Arneborg et al. (2007) speculated that the unusual three-layer transverse circulation (see Figure 2.8b) might be related to the effect of lateral density gradients. The direction of the near-bottom flow was found to be especially puzzling since, as argued above in the context of Figure 2.10a, the flow close to the bottom should be aligned with v_f and thus with the Ekman transport, and not opposite to it as observed. From their single-point measurements in the channel center alone, however, Arneborg et al. (2007) were not able to establish a connection between lateral density gradients and secondary circulation.

First direct evidence for the existence and potential importance of lateral density gradients was presented in Paper 2 by Umlauf et al. (2007), revealing the full complexity of the lateral density and velocity structure displayed in Figure 2.7. One important point emphasized by these authors was that in rotating flows such lateral density gradients are associated with a geostrophically balanced shear, commonly referred to as thermal wind shear, that follows from the z-derivative of (2.3):

$$\frac{\partial u_g}{\partial z} = -\frac{1}{f}\frac{\partial b}{\partial y} \quad . \tag{2.20}$$

In the cases considered here, the thermal wind shear below the interface has a tendency to

reduce down-channel speed towards the bottom in a purely inviscid way. Previous studies have pointed out that under these conditions "slippery" Ekman layers with vanishing bottom drag may be induced, obviously with serious consequences for flows that are frictionally controlled (MacCready and Rhines, 1993; Garrett et al., 1993). Although the strength of the lateral density gradients was found to be sufficient for the generation of slippery Ekman layers, direct stress measurements revealed, quite surprisingly, no indications for a reduction of bottom drag. This result was later confirmed by the model simulations in Paper 5 (Umlauf et al., 2010), which reproduced the generation of lateral buoyancy gradients but did not show evidence for a reduction of bottom drag either.

Umlauf and Arneborg (2009b) investigated this apparent inconsistency, pointing out that a major difference between the theory of MacCready and Rhines (1993) and the buoyancy-driven flows considered here is the presence of an along-flow pressure gradient. Umlauf and Arneborg (2009b) showed that in this case, instead of reducing the bottom drag, the flow reacts to lateral density gradients by generating a special type of secondary circulation required to balance the ageostrophic down-channel flow component. This is easiest understood by considering the cross-channel component of the momentum budget in (2.2), assuming stationary conditions and ignoring non-linear advection:

$$u - u_g = -\frac{1}{\rho_0 f}\frac{\partial \tau_y}{\partial z} \ , \tag{2.21}$$

where u_g is the geostrophically balanced down-channel speed defined in (2.3). Physically, (2.21) shows that the ageostrophic down-channel transport is compensated by the down-channel Ekman transport due to cross-channel stresses. Considering only regions close to the bottom, where the sign of τ_y is determined by the direction of the near-bottom flow, it is easy to show (Umlauf and Arneborg, 2009b) that for $u - u_g < 0$ the transverse velocity near the bottom is positive (to the right, looking upstream), while negative near-bottom speeds are observed for $u - u_g > 0$.

For the standard situation without lateral density gradients, $u < u_g$ is expected in the lower part of the gravity current due to the frictional reduction of u towards the bottom (Figure 2.13a). In this case, a positive transverse near-bottom flow will be observed. In the presence of lateral buoyancy gradients, however, u_g may decrease more rapidly towards the bottom than u such that a near-bottom layer with $u > u_g$ may exist (Figure 2.13b). In this case, the near-bottom transverse flow reverses sign and becomes negative, which Umlauf and Arneborg (2009b) showed to explain the puzzling structure of the secondary circulation observed in Figure 2.8. Further support for this argument came from the idealized numerical simulations by Umlauf et al. (2010), which were able to reproduce both the evolution of the lateral density gradient and the appearance of the three-layer structure of the secondary circulation (Figure 2.11b). Analysis of these model results confirmed the physical mechanisms described above as the reasons for the different structure of the secondary circulation in regions with and without lateral density gradients, respectively. Concluding, these results

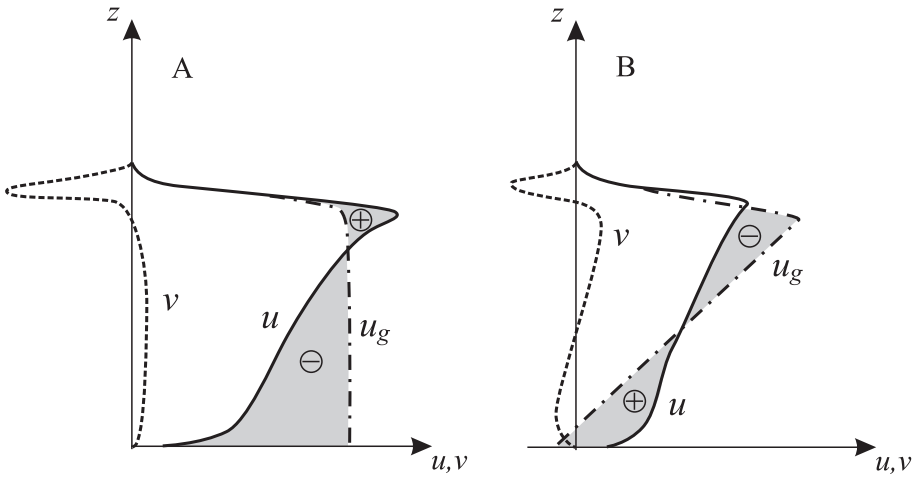

Figure 2.13: Conceptual picture for the dynamical effect of lateral density gradients: (a) situation without lateral stratification in the interior, and (b) with lateral stratification. Gray-shaded areas correspond to the ageostrophic component $u - u_g$ with sign as indicated. Modified figure from Umlauf and Arneborg (2009b).

have shown that a local imbalance in u and u_g triggers a secondary flow that provides the frictional forces required to close the momentum budget.

2.5.3 What we have learned

Figure 2.14 summarizes the main results from the preceeding sections in form of a conceptual picture for the dynamics of shallow, frictionally controlled gravity currents. Key dynamical component of these flows is an interfacial jet that, at least for the case of weak entrainment considered here, is geostrophically balanced by the pressure gradient arising from the down-channel tilt of the interface. Since, in frictionally controlled gravity currents, this pressure gradient is approximately balanced by the bottom stress, the latter also determines the strength of the jet. Umlauf and Arneborg (2009b) showed that this link between the bottom stress and the secondary circulation can be expressed in non-dimensional form in terms of the Ekman number E_k, which underlines the importance of this parameter for the parametrization of entrainment in frictionally controlled gravity currents. A connection between E_k and entrainment had already been deduced empirically from the results of the one-dimensional numerical model discussed in Paper 1 (Arneborg et al., 2007).

The transport q_i of interfacial fluid from right to left (looking upstream) leads to a pinching and spreading of interfacial isopycnals on opposite sides of the channel as illustrated in Figure 2.14. The compression of the interface on the right hand side makes it more amenable to shear instability, which led Umlauf and Arneborg (2009b) to speculate that the interfacial

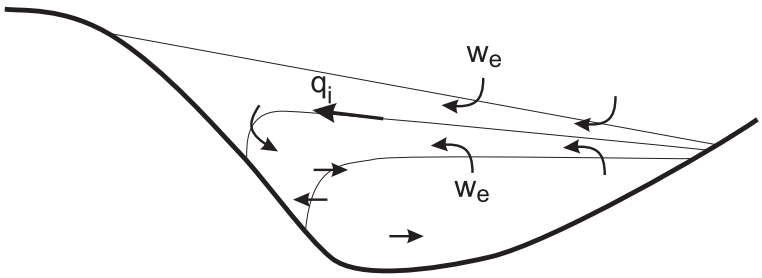

Figure 2.14: Conceptual sketch of secondary circulation and entrainment in a channelized, frictionally controlled gravity current. Modified figure from Umlauf and Arneborg (2009b).

transport q_i may be balanced by increased entrainment in this region. This was explicitly confirmed by the simulations in Paper 5 (Umlauf et al., 2010), showing that the interface on the right hand side of the channel is in a state of marginal stability with enhanced entrainment of fluid from above and below (Figure 2.14). This combination of interfacial mixing and secondary circulation was shown to result in a rather curious modification of the entrainment process (Figure 2.15): ambient fluid entrained into the interface on the right hand side of the channel is fed into the jet, and then transported with the jet to the opposite side of the channel, where it is finally mixed down into the interior (Umlauf et al., 2010). This questions the traditional view of entrainment as a strictly one-dimensional process that can be described by local (in the lateral sense) bulk parameters like the Froude number.

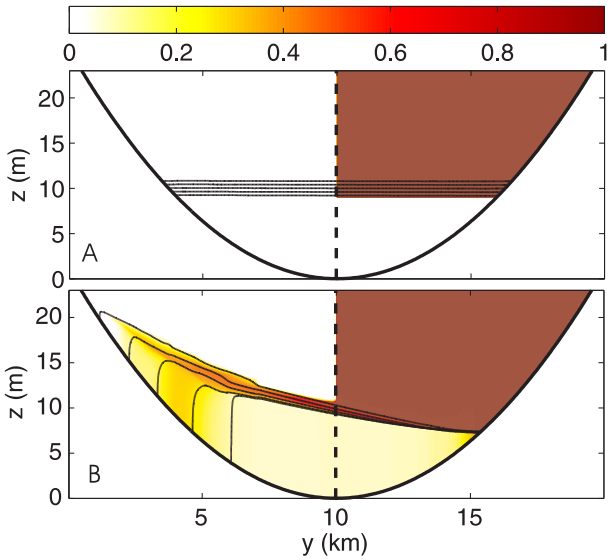

Figure 2.15: Density structure (thin black lines), and concentration of a passive tracer (a) at the start of the simulation, and (b) after two intertial periods. The simulation is idential to that shown in Figure 2.11. Modified figure from Umlauf et al. (2010).

The interior region below the interface was found to be separated into two dynamically different regions: an unstratified region on the right hand side of the flow (looking upstream), and a region with nearly vertical isopycnals on the left, creating a lateral density gradient (see Figure 2.14). The secondary circulation in the unstratified region was shown to be weak due to the fact that geostrophically balanced and Ekman-related transverse velocities nearly cancel (Papers 3 and 4 by Umlauf and Arneborg, 2009a,b). Dynamically more interesting is the region with lateral density gradients in the interior below the interface. Previous theoretical work on the dynamics of bottom boundary layer flows along sloping topography has shown that such lateral stratification may be associated with a reduction of the bottom drag, generating what has been called "slippery" Ekman layers (MacCready and Rhines, 1993; Garrett et al., 1993). It is tempting to assume that a similar effect also occurs in gravity currents with lateral density gradients, and some related speculations have in fact been made by Paka et al. (1998) for the Stolpe Channel overflow in the Central Baltic Sea. Surprisingly, however, for the flows considered here, neither observations nor simulations showed any indications for a modification of the bottom drag in the presence of lateral density gradients, although the thermal wind shear associated with the latter was found to be comparable to the total observed vertical shear. Instead of reducing the bottom drag, frictionally controlled gravity currents were shown to respond to the presence of lateral density gradients with the generation of a near-bottom reversal of the transverse flow. Near-bottom velocities oppose the bottom Ekman transport, and adjust exactly such that the ageostrophic component of the down-channel flow is balanced (Umlauf and Arneborg, 2009b; Umlauf et al., 2010).

The gravity currents studied in this work are characterized by low Froude numbers, weak entrainment, confinement by lateral topography, and particularly by their shallowness compared to the thickness of the bottom Ekman layer. Flows of this type have been reported for numerous locations also beyond the Baltic Sea, most notably in the context of the small-scale gravity currents transporting dense water down the continental slopes inside narrow canyons or along submarine ridges (Kämpf, 2000; Foldvik et al., 2004; Darelius, 2008). It is likely that the theoretical framework developed in Papers 1-5 will be of some relevance also for the interpretation of these ubiquitous flows that are suspected to be essential for the deep-water formation process in the ocean.

In contrast to these shallow gravity currents, large-scale oceanic overflows often exhibit a thickness that is comparable to or larger than the Ekman layer thickness, which reduces the Ekman number and thus the relative importance of frictional effects. This "gray zone" between frictional and hydraulic theory has received very little attention so far although it forms an important hybrid case that is perhaps of greatest relevance for real oceanic overflows. This has also become evident in a recent study by Cuthbertson et al. (2011), who investigated laboratory-scale gravity currents inside a topographic constriction, showing a puzzling consistency of their measurements with both hydraulic and frictional theory.

Similarly, recent investigations of gravity currents in the Stolpe Channel, the largest overflow site in the Baltic Sea, revealed a behavior that was in perfect agreement with the frictional theory presented above (e.g., regarding the lateral density structure) — but showed at the same time memory of upstream potential vorticity that explained the meandering of the flow (Zhurbas et al., 2012). Analogous findings have been reported for the Faroe Bank Channel overflow that showed features explainable from rotating hydraulics (Lake et al., 2005; Darelius et al., 2011), and others, like the secondary circulation, that point towards the importance of the same frictional effects that have been analyzed in this chapter (Johnson and Sanford, 1992; Seim and Fer, 2011). Future work will hopefully be able to provide a sound theory combining these two crucial aspects of rotating bottom gravity currents.

Chapter 3

Internal structure and dynamics of sloping boundary layers

3.1 Introduction

In the second part of this work, the focus will be on the dynamics and internal structure of bottom boundary layers (BBLs) driven by long internal-wave motions in stratified basins. The discussion will be centered around the processes occurring inside the lowermost, nearly well-mixed part of the BBL that has been shown to be particularly relevant for net basin-scale mixing and energy dissipation in small to medium-sized stratified basins such as lakes and fjords (Wüest and Lorke, 2003; Wüest et al., 2000; Goudsmit et al., 1997). This situation is somewhat different from larger (ocean) basins, where layers with enhanced turbulence levels, driven by breaking internal waves, have been shown to extend far beyond the homogeneous near-bottom layer into the stratified interior (Rudnick et al., 2003; Nash et al., 2007; Kunze et al., 2012). This process is known to be both highly energetic and efficient, and may therefore overwhelm the contribution of diapycnal mixing in the lower, weakly stratified part of the BBL. Nevertheless, there is observational evidence that the creation of gravitationally unstable BBLs described in the following is also relevant in the ocean, however, with a strong modification due to rotational (Ekman) effects (Moum et al., 2004).

The investigations discussed in Papers 8-11 were motivated by a new type of boundary mixing process first identified in a small Swiss lake (Lake Alpnach), in which near-bottom currents are driven by internal seiching motions (Lorke et al., 2005). These data suggested that differential advection of isopycnals due to the slope-normal shear modifies the stratification inside the BBL as schematically illustrated in Figure 3.1 for the case without rotation. During periods of up-slope flow (Figure 3.1a), dense water may be advected on

top of light water — with immediate consequences for mixing due to the onset of convection. During periods of down-slope flow, differential advection has a tendency to create stable stratification inside the BBL (Figure 3.1b), which will impact on turbulence in at least two competing ways: (a) by reducing both the length scale and the kinetic energy of turbulent fluctuations, and (b) by increasing the efficiency of mixing. The overall effect on mixing has been unclear. It is worth noting that this shear-driven periodic generation and destruction of stratification is qualitatively similar to the process of tidal straining observed in estuaries and regions of fresh-water influence. In this case, tidal currents drive a lateral density gradient over flat bottom, which may lead to unstable stratification and convection during flood, and to the creation of stable stratification during ebb (Simpson et al., 1990; Burchard et al., 2001). While the interest in tidal straining has been motivated mainly by its importance for the horizontal residual transports (Jay and Musiak, 1994; Burchard and Hetland, 2010), shear-induced convection near sloping topography is likely to be relevant in view of its role for net diapycnal mixing.

Although Lorke et al. (2005) could clearly identify the processes delineated above in their data, they were not able to find a generally valid relation between the outer parameters of the problem (slope angle, bottom roughness, ambient stratification, etc.), and the parameters that quantify boundary mixing (buoyancy flux, dissipation rate, turbulent diffusivity, etc.). Therefore, no definite conclusions could be drawn about the relevance of their observations for other locations in the lake, or even for other stratified basins. Moreover, the question about the contribution of BBL mixing to net basin-scale mixing turned out to be difficult to answer because the vertical turbulent buoyancy flux, a frequently used indicator for "mixing" in stably stratified flows, changes sign inside the convective layers, which complicates its straightforward interpretation.

These questions were addressed in a recent research project aimed at the "Quantification of Shear-Induced Convection and Bottom-Boundary Mixing in Natural Waters" (ShIC), funded by the German Research Foundation (DFG). The following summary of the main results starts with Paper 8 by Lorke et al. (2008) that describes an extensive field program in a large fresh-water lake, focusing on the direct observation of turbulence parameters in gravitationally unstable BBLs. Paper 9 by Umlauf and Burchard (2011) contains a combined theoretical-numerical study, in which the reasons for and consequences of shear-induced convection in BBLs are investigated in the framework of an idealized one-dimensional geometry. Finally, in the two companion papers 10 and 11 (Becherer and Umlauf, 2011; Lorrai et al., 2011), the full three-dimensional problem is studied with the help of a high-resolution numerical model of Lake Alpnach. Besides the analysis of the basin-scale internal wave field, these two papers also contain a direct comparison of modeled and observed BBL properties, using data from different years and different locations on the slopes of the lake.

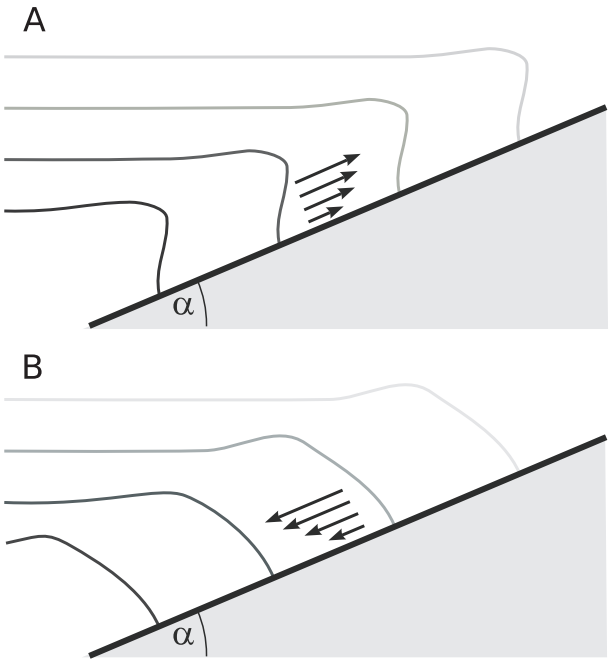

Figure 3.1: Conceptual picture of mixing near sloping topography in the presence of oscillatory up- and down-slope flow. (a) Creation of unstable stratification (convection) during up-slope flow, and (b) stabilization during down-slope flow. Rotation and Ekman effects are ignored.

3.2 Observations in Lake Constance

To obtain broader observational support for the processes sketched in Figure 3.1, the measurements in Lake Alpnach were extended to a second study site with rather different characteristics (see Paper 8 by Lorke et al., 2008). Lake Constance, one of the largest and deepest lakes in Western Europe, consists of an approximately 40 km long and 250 m deep main basin, to which an elongated approximately 20 km long side basin is attached (Figure 3.2). Typical for this lake is the presence of regular internal seiching motions during the summer months that exhibit periods of 3-5 days, and dominate the near-bottom currents throughout the lake (Appt et al., 2004; Lorke et al., 2008). The different geometry and size compared to Lake Alpnach, and the considerably longer forcing period for the near-bottom currents, suggested a different parameter range that was assumed to provide a useful test for the robustness of the BBL mixing processes described above. The study site was located on the slope of the north-western appendix of Lake Constance that is usually referred to as Lake Überlingen (Figure 3.2). This site was chosen primarily due to its location on the gently sloping end of the channel that is usually affected by strong and regular internal seiching motions, and because rotational effects were expected to be small due to the small lateral scales of the appendix. This is different for the main basin of Lake Constance, where

internal seiching is known to occur in form of a Kelvin-type wave propagating cyclonically along the shoreline (Appt et al., 2004).

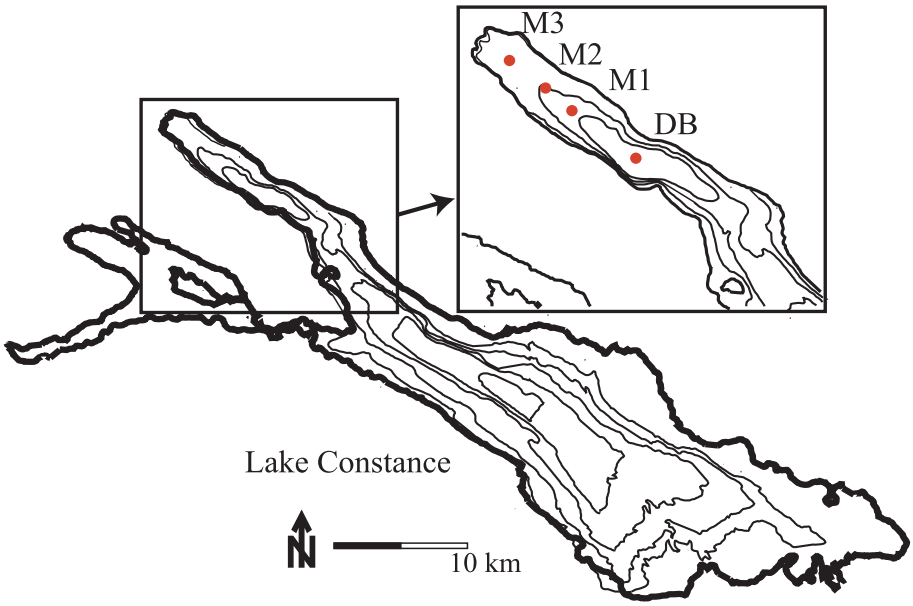

Figure 3.2: Map of Lake Constance with topography at 50 m intervals (maximum depth is 250 m). Inset map shows Lake Überlingen with mooring positions indicated. Lake Constance is located between Germany, Switzerland, and Austria at approximately 47°37'N, 19°22'E. Modified figure from Lorke et al. (2008).

Lorke et al. (2008) discussed data from mooring position M2 (Figure 3.2) during two times of the seiching cycle with up- and down-slope flow, respectively. Similar to Lake Alpnach, the BBL was found to become gravitationally unstable inside a near-bottom region of up to 4 m thickness during up-slope flow, whereas during down-slope flow the BBL remained stable (Figure 3.3). A more detailed analysis in Paper 8 showed that the reasons for these effects were perfectly consistent with the schematic picture outlined above, providing further evidence for the relevance of shear-induced convection in lakes. Measurements using a Doppler velocimeter (ADV) combined with a fast-response thermistor, both mounted on a bottom-frame at position M2, showed that the magnitudes of the dissipation rate and the vertical turbulent buoyancy flux were comparable during the stable and unstable periods. The buoyancy flux, however, reversed direction during the unstable phases, which provided the first direct evidence for the presence of turbulent convection. During these periods, the turbulent diffusivity increased by almost an order of magnitude, and it appeared tempting to interpret this as an indication for the importance of convection for net vertical mixing. Surprisingly, however, the results discussed in the following showed that the opposite is the case.

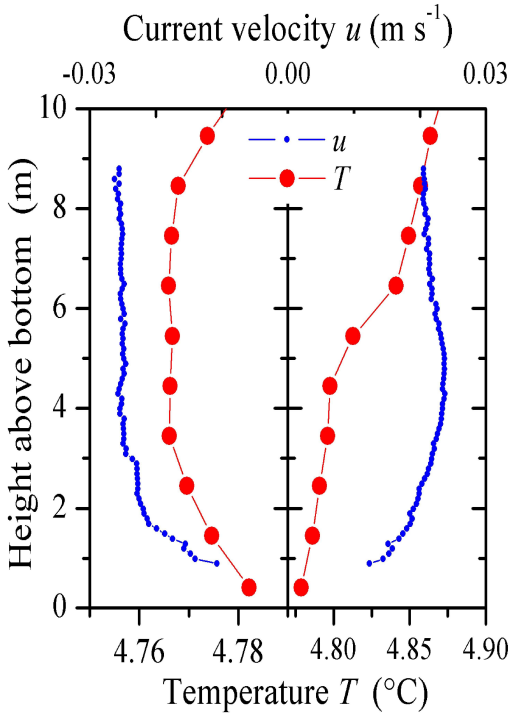

Figure 3.3: Near-bottom velocity (blue) and temperature (red) from a thermistors chain and a current profiler located at position M2 (see Figure 3.2). Observations are shown for two times during the seiching cycle with up-slope (left) and down-slope velocities, respectively. Note the unstable stratification during up-slope flow. Modified figure from Lorke et al. (2008).

3.3 Theory and one-dimensional analysis

3.3.1 Geometry and governing equations

Assuming that stratification outside the BBL is strictly vertical and homogeneous, that the slope is uniform, and that flow variations in the up-slope direction can be ignored, the boundary-mixing problem becomes one-dimensional in a tilted coordinate system aligned with the slope as depicted in Figure 3.4. The price for the attractive simplicity of this one-dimensional framework is the elimination of some important processes, e.g. internal-wave motions and the exchange of fluid between the BBL and interior by intrusions. Previous studies have nevertheless shown that useful conclusions can be drawn from this type of models regarding the interaction of stratification, secondary circulation, and mixing inside the BBL (e.g., Phillips, 1970; Thorpe, 1987; Garrett, 1990). The more general three-dimensional case will be investigated in the summary of Papers 10 and 11 in Section 3.4.

Starting from the one-dimensional geometry shown in Figure 3.4, in Paper 9 Umlauf and

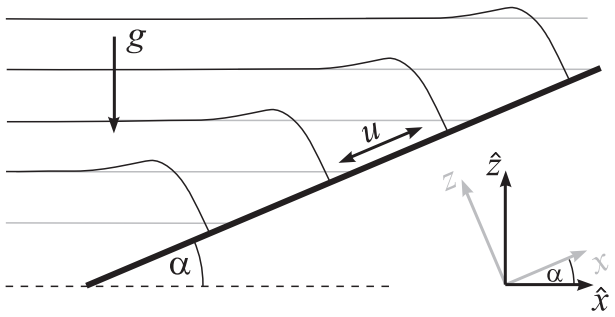

Figure 3.4: Geometry of a BBL on a uniform slope with slope angle α. Thin lines denote isopycnals, $\boldsymbol{g}$ is the gravitational acceleration. Note that the geometry becomes one-dimensional in the tilted coordinate system (x, z). Modified figure from Umlauf and Burchard (2011).

Burchard (2011) considered a Boussinesq fluid periodically moving up and down a uniform slope with slope angle α in an infinitely deep basin with variable stratification,

$$N^2 = \frac{\partial b}{\partial \hat{z}} \quad . \tag{3.1}$$

Here, using the notation from Paper 9, $\hat{z}$ denotes the vertical coordinate (see Figure 3.4), and b the buoyancy defined as

$$b = -g\frac{\rho - \rho_0}{\rho_0} \, , \tag{3.2}$$

where ρ denotes density, ρ_0 a constant reference density, and g the acceleration of gravity. Outside the BBL, isopycnals are assumed to be perfectly horizontal, and stratification is constant ($N = N_\infty$). Focusing on boundary mixing in small lakes, Umlauf and Burchard (2011) ignored Earth's rotation, pointing out, however, that the theoretical framework is easily extended to include rotational effects.

In Paper 9, it was shown that under the above assumptions the Boussinesq equations in tilted coordinates (see Figure 3.4) can be written as:

$$\begin{aligned} \frac{\partial u}{\partial t} &= (b - b_\infty)\sin\alpha + \frac{\partial u_\infty}{\partial t} - \frac{1}{\rho_0}\frac{\partial \tau_x}{\partial z} \, , \\ \frac{\partial b}{\partial t} &= -uN_\infty^2 \sin\alpha - \frac{\partial G}{\partial z} \, , \end{aligned} \tag{3.3}$$

where τ_x and G denote the slope-normal turbulent momentum and buoyancy fluxes, respectively (the turbulent fluxes parallel to the slope are ignored). The undisturbed buoyancy is denoted by b_∞, which may vary due to advection, however, only under the constraint that $N_\infty^2 = \partial b_\infty / \partial \hat{z}$ remains constant everywhere. The first term on the right hand side of the momentum budget in (3.3) therefore represents the baroclinic pressure gradient set up by the tilting of isopycnals in the BBL due to mixing and frictional effects (see Figure 3.4). The function u_∞ represents the (prescribed) external pressure forcing, e.g. due to long

internal waves or basin-scale internal seiches. As the most simple representation of periodic internal-wave forcing, Umlauf and Burchard (2011) assumed a purely harmonic dependency:

$$u_\infty = U \sin \omega t \ , \tag{3.4}$$

where U denotes a constant velocity scale, and ω the constant forcing frequency. The first term on the right hand side of the buoyancy equation in (3.3) represents up-slope advection of buoyancy, which can be understood from the fact that $N_\infty^2 \sin\alpha$ coincides with the (constant) up-slope buoyancy gradient $\partial b/\partial x$ (see Paper 9). Finally, no-slip, insulating boundary conditions are assumed at the slope:

$$u = 0 \ , \quad \frac{\partial b}{\partial z} = 0 \qquad \text{for} \quad z = 0 \quad . \tag{3.5}$$

The turbulent slope-normal fluxes appearing in (3.3) are computed from down-gradient formulations of the form:

$$\frac{\tau_x}{\rho_0} = \left\langle u'w' \right\rangle = -\nu_t S \ , \quad G = \left\langle w'b' \right\rangle = -\nu_t^b \check{N}^2 \ , \tag{3.6}$$

where primes denote turbulent fluctuations, and angular brackets the Reynolds average. $S = \partial u/\partial z$ and $\check{N}^2 = \partial b/\partial z$ are the slope-normal shear and buoyancy gradient, respectively. Is is worth noting that the latter is different from the vertical buoyancy gradient N^2 such that the terms well-mixed ($\check{N}^2 = 0$) and unstratified ($N^2 = 0$) do not exactly coincide (Umlauf and Burchard, 2011). For the assumed mild slopes ($\alpha \ll 1$), however, this difference only matters for the precise timing of the onset of convection near the transition from stable to unstable stratification.

The turbulent diffusivities ν_t and ν_t^b appearing in (3.6) are derived from the second-moment turbulence model already outlined in Chapter 2 in the context of (2.6). This model follows the detailed description in Paper 6 (Umlauf and Burchard, 2005), however, with the following caveat. The boundary-layer assumption used in the model derivation in Paper 6 explicitly assumes that the turbulent fluxes represented by the model are strictly vertical, which conflicts with the interpretation of τ_x and G as slope-normal fluxes used here. Umlauf and Burchard (2011) pointed out, however, that these differences become negligible for $\alpha \ll 1$, which was always insured for the cases considered in Paper 9. For small slopes, it it also likely (though it cannot be proven) that the up-slope turbulent fluxes can be ignored, as assumed in the following (Umlauf and Burchard, 2011).

3.3.2 Analysis of model results

Some results of this model, taken from Paper 9 by Umlauf and Burchard (2011), are displayed in Figure 3.5. This figure shows the evolution of velocity, buoyancy, and stratification over two forcing periods after periodic conditions have been reached. The forcing period

in (3.4) was chosen as $T_f = 2\pi/\omega = 12.4$ hours for this example, which corresponds to the M_2 tidal period, and is also of the order of typical internal seiching periods in small to medium-sized lakes. The forcing amplitude was set to $U = 0.05$ m s^{-1}, and slope angle and interior stratification were taken to be $\alpha = 10^{-2}$ and $N_\infty^2 = 10^{-5}$ s^{-2}, respectively, corresponding to typical values in marine and limnic environments (Umlauf and Burchard, 2011). A wider parameter space is discussed below.

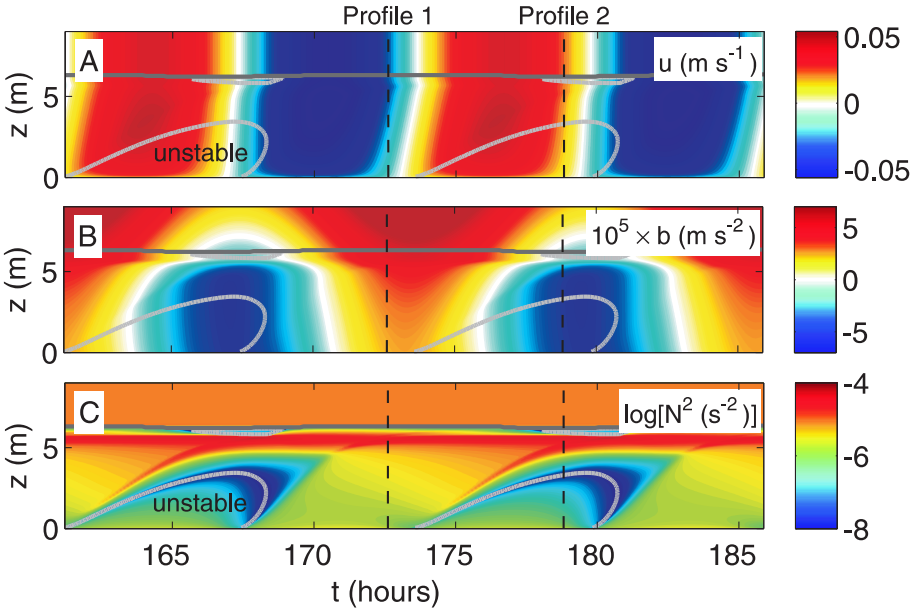

Figure 3.5: Evolution of (a) velocity, (b) buoyancy, and (c) absolute value of the square of the buoyancy frequency over two forcing periods. The dark gray lines denote the upper limit of the BBL, and the light gray lines include unstable near-bottom regions. The abscissa corresponds to time after model start from rest. Results shown here correspond to fully periodic conditions. Modified figure from Umlauf and Burchard (2011)

The velocity in the BBL (Figure 3.5a) is seen to closely follow the periodic forcing, however, with a reduction and small phase lead towards the bottom, both consistent with the increasing importance of frictional effects. The evolution of buoyancy (Figure 3.5b) is dominated by the up- and down-slope advection of stratification, which is completely analogous to the periodic warming and cooling patterns observed on the slopes of the lakes studied in this project (Lorke et al., 2008; Lorrai et al., 2011). The stratification shown in Figure 3.5c illustrates that the BBL is separated from the interior by a permanent pycnocline that is a direct manifestation of enhanced boundary mixing. Most importantly, however, and analogously to the observations discussed above, stratification inside the BBL periodically varies between stable and unstable conditions, corresponding to periods with down- and up-slope flow, respectively. Umlauf and Burchard (2011) derived an evolution equation for N^2, and showed that the physical mechanisms leading to these alternating patterns of stratification

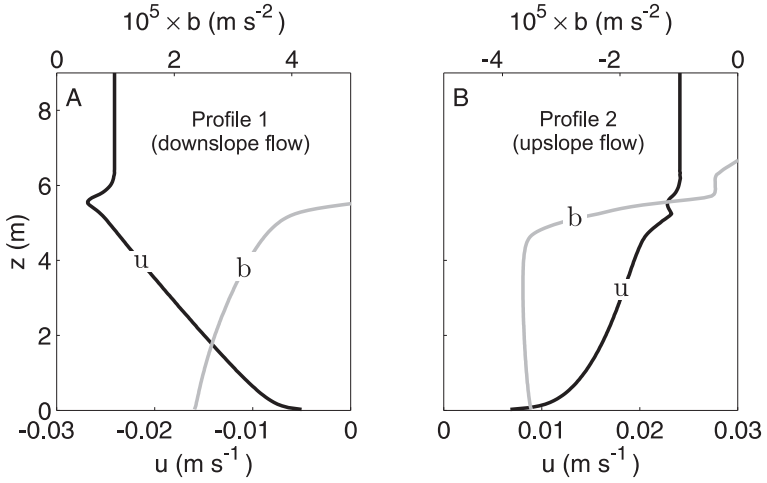

Figure 3.6: Profiles of velocity and buoyancy for the two times indicated in Figure 3.5. Modified figure from Umlauf and Burchard (2011).

were exactly those outlined above in the context of Figure 3.1. Two profiles of velocity and buoyancy, approximately corresponding to the times of strongest stable and unstable stratification, respectively, are shown in Figure 3.6. Comparison with the measurements in Lake Constance in Figure 3.3 reveals a strong qualitative similarity, noting that temperature and buoyancy anomalies are related in an approximately linear way. From these results, Umlauf and Burchard (2011) concluded that their simple one-dimensional model reproduces the basic mechanisms of shear-induced stabilization and destabilization of the BBL.

The impact on turbulence of the transition from stable to unstable conditions is immediately evident from the turbulent buoyancy flux shown in Figure 3.7a: while in stable regions the buoyancy flux is downward, in unstable regions it reverses sign, indicating the onset of convection. Umlauf and Burchard (2011) pointed out that this effect questions the usual approach for the quantification of boundary mixing, in which an "effective" diffusivity is computed by horizontally averaging the vertical buoyancy flux across the BBL, and dividing the result by some representative interior value for N^2 (in this case N^2_∞). In the presence of convection, however, where the buoyancy flux changes sign, this method results in negative effective diffusivities that have no physical interpretation. Moreover, Umlauf and Burchard (2011) showed that the secondary circulation inside the BBL leads to a net *advective* contribution to the total vertical buoyancy flux that has a tendency to re-stratify the BBL. This advective counter-gradient flux partly compensates the turbulent buoyancy flux, thus reducing the effective diffusivity.

For the simple geometry considered here, Umlauf and Burchard (2011) derived an exact equation for the total (i.e. advective plus turbulent) irreversible buoyancy flux, and showed

it to be proportional to the time-average of the integrated mixing rate,

$$X_b = \int_0^\infty \chi_b \, \mathrm{d}z \; , \quad \chi_b = 2\nu^b \left\langle \frac{\partial b'}{\partial x_i} \frac{\partial b'}{\partial x_i} \right\rangle \tag{3.7}$$

where ν^b is the molecular diffusivity of buoyancy (corresponding to that of either heat or salt). χ_b is recognized as the small-scale destruction of buoyancy variance due to molecular mixing, which is one of the key parameters in stratified turbulence (Tennekes and Lumley, 1972). The relation found by Umlauf and Burchard (2011) therefore links small-scale mixing to large-scale changes in background potential energy via the net irreversible buoyancy flux. The mixing rate defined in (3.7) is accessible to both turbulence modeling and turbulence microstructure observations.

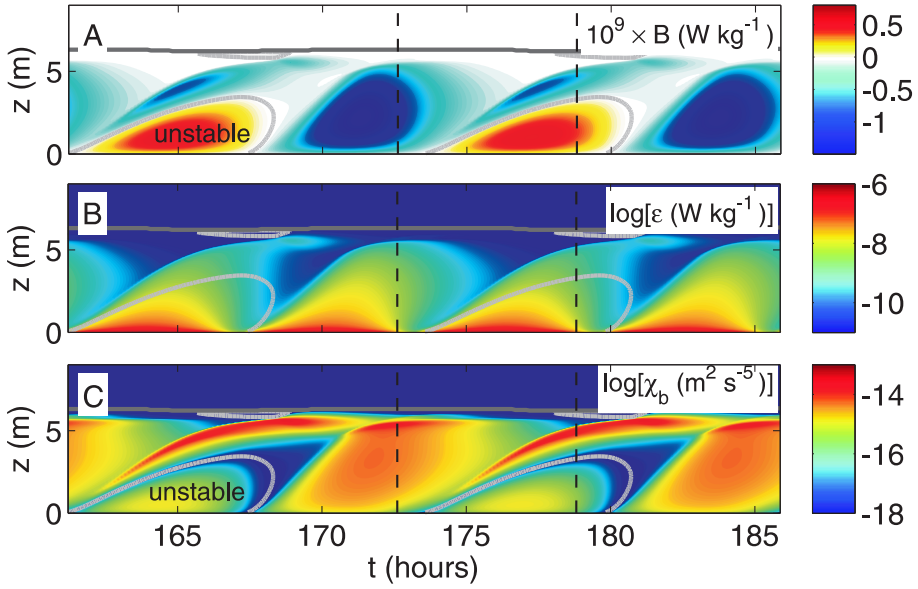

Figure 3.7: As in Figure 3.5 but now for (a) the turbulent buoyancy flux, (b) the rate of dissipation, and (c) the molecular destruction of buoyancy variance. Modified figure from Umlauf and Burchard (2011).

Comparing the evolution of the dissipation rate ε (Figure 3.7b) with that of the mixing rate χ_b (Figure 3.7c) reveals rather different patterns. While the periodic variations of ε appear to be only weakly affected by the alternating patterns of stable and unstable stratification, the behavior of the mixing rate χ_b exhibits a strong asymmetry. Mixing is seen to be largely confined to periods of down-slope flow, where shear creates stable stratification that allows for an efficient conversion of turbulent kinetic to potential energy. This is contrasted by the behavior of the gravitationally unstable layers, which are characterized by high energy dissipation but weak mixing. A more detailed analysis in Paper 9 showed that the contribution of mixing in these regions is negligible. These results clearly demonstrate that the standard approach of relating the local buoyancy flux to the dissipation rate via

a constant mixing efficiency (Osborn, 1980) is not a good choice for the interpretation of boundary-layer mixing data.

3.3.3 Non-dimensional description

To generalize these results for a larger parameter space, Umlauf and Burchard (2011) derived non-dimensional expressions for the momentum and buoyancy equations in (3.3), as well as for the corresponding boundary conditions and the transport equations in the turbulence model described in Paper 6 (Umlauf and Burchard, 2005). In spite of the complexity of this coupled problem, the solution could be shown to depend only on the following three non-dimensional parameters: the slope angle α, the non-dimensional forcing frequency $\Omega = \omega/N_\infty$, and a "roughness number" defined as $R = z_0 N_\infty / U$, where z_0 denotes the bottom roughness introduced by the boundary conditions. The physically interesting range spanned by these three parameters was explored with the help of the numerical model described above. As one important qualitative result, Umlauf and Burchard (2011) pointed out that "in all our simulations we observed periods with unstable boundary layers, suggesting that this phenomenon is an intrinsic component of the BBL dynamics, at least in the non-rotating case". This finding is consistent with the three-dimensional simulations described below, and illustrates the ubiquitous nature of shear-induced convection in non-rotating BBLs.

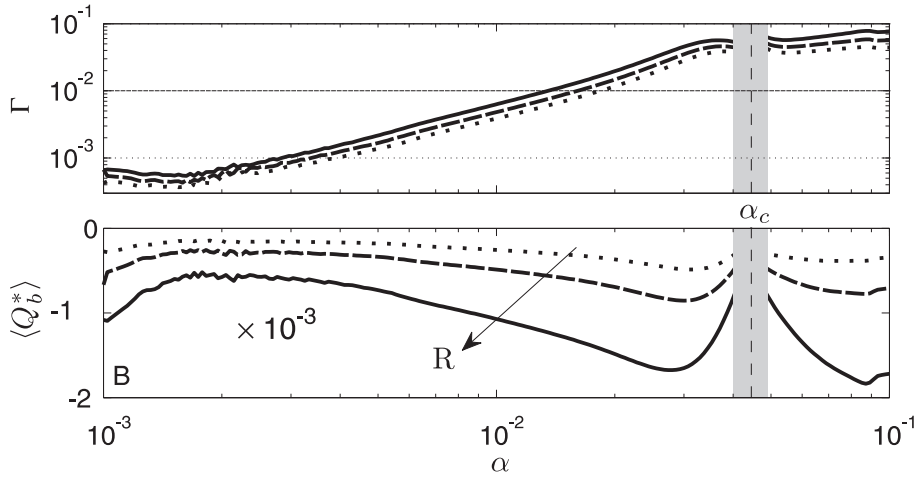

Figure 3.8: (a) Total mixing efficiency Γ, and (b) non-dimensional vertical buoyancy flux $\langle Q_b^* \rangle$ as functions of the slope angle α. Results are shown for $\Omega = 4.5 \times 10^{-2}$ and $R = 6.3 \times 10^{-5}$ (dashed line), both corresponding to the example shown in Figure 3.5. Also shown are cases with larger ($R = 6.3 \times 10^{-4}$, solid line) and smaller ($R = 6.3 \times 10^{-6}$, dotted line) roughness numbers. Regions in the vicinity of the critical slope α_c are blanked. Modified figure from Umlauf and Burchard (2011).

In Paper 9, it was also shown that the relevant parameter for the quantification of the net

effect of boundary mixing is the total vertical buoyancy flux $\langle Q_b \rangle$, corresponding to the sum of the turbulent and advective fluxes, averaged over one forcing period, and integrated horizontally across the BBL. This crucial parameter, quantifying the total irreversible change of potential energy due to mixing, was made dimensionless with the help of the forcing speed U, resulting in $\langle Q_b^* \rangle = \langle Q_b \rangle U^{-3}$. Dividing this quantity by the dissipation rate, averaged and integrated in the same way, yields the total efficiency Γ of boundary mixing. Umlauf and Burchard (2011) argued that for periodic conditions, $\langle Q_b^* \rangle$ and Γ, as well as any other non-dimensional bulk variable, can only be functions of the non-dimensional parameters α, R, and Ω identified above. These functional dependencies for the physically interesting range of α and R are shown in Figure 3.8, where Ω is kept fixed at the value corresponding to the example discussed above (see Figure 3.5). Note that for the critical angle $\alpha_c = N_\infty \sin \alpha$, that happens to coincide with the angle for critical reflection of internal waves, the boundary layer shows resonance with the imposed forcing (Umlauf and Burchard, 2011). These regions are blanked in Figure 3.8 because the physical significance of the solutions becomes questionable in the vicinity of α_c due to the geometric limitations of the model.

The mixing efficiency (Figure 3.8a) is seen to strongly increase with increasing slope angle, reaching values of a few percent for slopes steeper than $\alpha = 10^{-2}$. Umlauf and Burchard (2011) showed that this behavior can be explained by a stronger tendency for BBL re-stratification on steeper slopes. Overall, mixing efficiencies are considerably smaller than the canonical value of $\Gamma = 0.2$, leading to the conclusion that boundary mixing, as represented by the simple model discussed here, is a rather inefficient process. Umlauf and Burchard (2011) noted, however, that in their one-dimensional simulations, no exchange of fluid between the BBL and the interior via intrusions is permitted, which eliminates one important process for boundary-layer restratification that is likely to be associated also with an increase in the mixing efficiency (Armi, 1978, 1979). This is confirmed by the three-dimensional simulations discussed in Section 3.4 below that show substantially higher mixing efficiencies.

One interesting result pointed out in Paper 9 is the fact that the non-dimensional buoyancy flux shown in Figure 3.8b varies only by a factor 2-3 over a range of two orders of magnitude for the slope angle. Greater roughness (i.e., increasing R) is seen to lead to stronger buoyancy fluxes (Figure 3.8b), and higher mixing efficiencies (Figure 3.8a), with an overall effect on mixing that is, however, substantially smaller than that due to variations in bottom slope. The overall conclusion from this is that, to first order, the non-dimensional integrated buoyancy flux can be assumed to be constant with $\langle Q_b^* \rangle \approx 10^{-3}$. This important result suggests that the net irreversible vertical buoyancy flux, horizontally integrated over the BBL, scales as U^3.

3.4 Three-dimensional analysis

Paper 10 (Becherer and Umlauf, 2011) and Paper 11 (Lorrai et al., 2011) describe the extension of these idealized, one-dimensional investigations to a three-dimensional natural system. Study area for this part of the project was Lake Alpnach (Switzerland), a small alpine lake that has been focus of numerous previous studies of seiching-induced boundary mixing (e.g., Goudsmit et al., 1997; Gloor et al., 2000; Lorke et al., 2002). Lake Alpnach (Figure 3.9) is an approximately 4-5 km long, elongated basin, located in a narrow alpine valley that is meteorologically characterized by diurnal thermal winds blowing along the major axis of the lake during the summer months. Previous studies (Münnich et al., 1992) have demonstrated that these periodic winds resonantly excite vertical mode-2 internal seiches with 24-hour period that provide the main energy source for boundary mixing. Based on data from Lake Alpnach, Lorke et al. (2005) reported first evidence for the generation of shear-induced convection in the BBL of a lake, which has motivated much of the work discussed in this chapter.

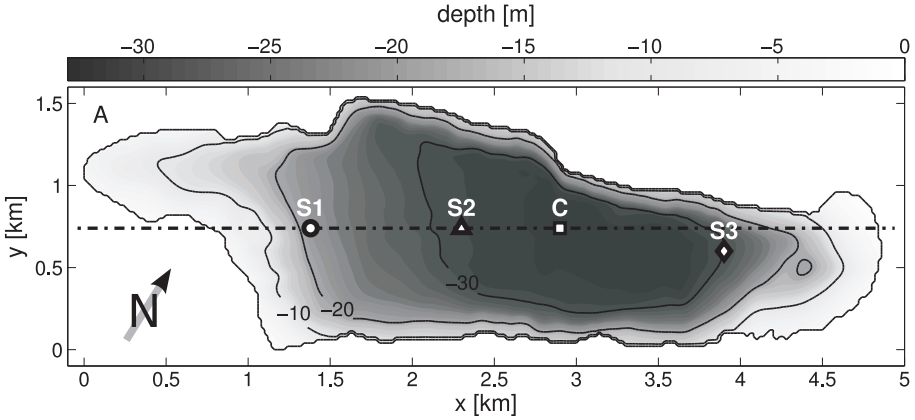

Figure 3.9: Topography of Lake Alpnach. The dash-dotted line denotes the position of the transect shown in Figure 3.10. Markers correspond to locations discussed in Paper 10 by Umlauf and Burchard (2011).

In Paper 10, Becherer and Umlauf (2011) used a high-resolution three-dimensional numerical model, based on the hydrostatic Boussinesq equations, in order to study these boundary mixing processes in greater detail. The model employs terrain following coordinates, allowing to resolve the complete range of relevant scales from the small-scale vertical structure of shear and stratification inside the BBL up to the largest scales associated with the basin-scale internal seiching motions. The effect of unresolved turbulent motions was parametrized with the help of the turbulence model described in Paper 6 (Umlauf and Burchard, 2005), which is identical to that used for the gravity current studies in Chapter 2 and the one-dimensional BBL simulations in Section 3.3 above. A detailed model description and numerical imple-

mentation details are given in Paper 10, and in the model documentation by Burchard and Bolding (2002, also see http://www.getm.eu).

3.4.1 Boundary-layer dynamics

In their idealized simulations, aimed at understanding the mechanisms and spatial distribution of boundary mixing in the presence of three-dimensional topography, Becherer and Umlauf (2011) assumed a sinusoidal wind forcing with a period of $T_f = 24$ hours as the most simple representation of the thermally-forced diurnal wind field over the lake. The wind stress was assumed to be spatially homogeneous, pointing along the major axis of the lake, and all other atmospheric fluxes were ignored (which is justified by the short simulation period and the interest in deep-water processes only). The velocity and density structure from these simulations is shown in Figure 3.10. Approximately two days after the onset of the periodic wind forcing, the water column in the central part of the lake is seen to be dominated by motions with diurnal frequency that Becherer and Umlauf (2011) identified as the resonantly excited vertical mode-2 internal seiches, in close agreement with previous observations (Münnich et al., 1992; Lorke et al., 2005). The structure of these standing internal waves in a transect along the major axis of the lake is shown Figure 3.10b-e for different times during one seiching cycle. The lateral velocity structure and the characteristic isotherm compression and expansion patterns at opposing ends of the lake were found to be consistent with horizontal mode-1 motions (Münnich et al., 1992). Becherer and Umlauf (2011) showed that the velocities associated with these internal motions dominate the near-bottom shear, suggesting them as the main driving factor for boundary mixing. Different from previous studies that have ignored the effect of rotation on internal seiching in Lake Alpnach, Becherer and Umlauf (2011) found that vertical mode-2 motions exhibit the characteristics of a Kelvin-type wave propagating cyclonically around the perimeter of the basin with slightly decreasing signal strength towards the center. Nevertheless, the periodic near-bottom currents induced by these seiching motions on the two main slopes of the lake (positions S1 and S3 in Figure 3.9) were found to be largely cross-isobath, such that the basic mechanisms sketched in Figure 3.1 still applied.

Taking position S3 as an example, Becherer and Umlauf (2011) showed that the BBL does indeed become gravitationally unstable during periods of up-slope flow. Completely analogous to the one-dimensional simulations discussed in Section 3.3, a reversal of the turbulent buoyancy flux is observed that indicates the onset of convection. In spite of large diffusivities during these convective periods, the mixing rate defined in (3.7) was found to be negligible due to the vanishingly small temperature gradients in the convective regions. As in the one-dimensional simulations discussed above, overall BBL mixing at position S3 was found to occur during periods of down-slope flow. The most significant difference compared to the one-dimensional case was related to the cross-slope advection of stratification, and

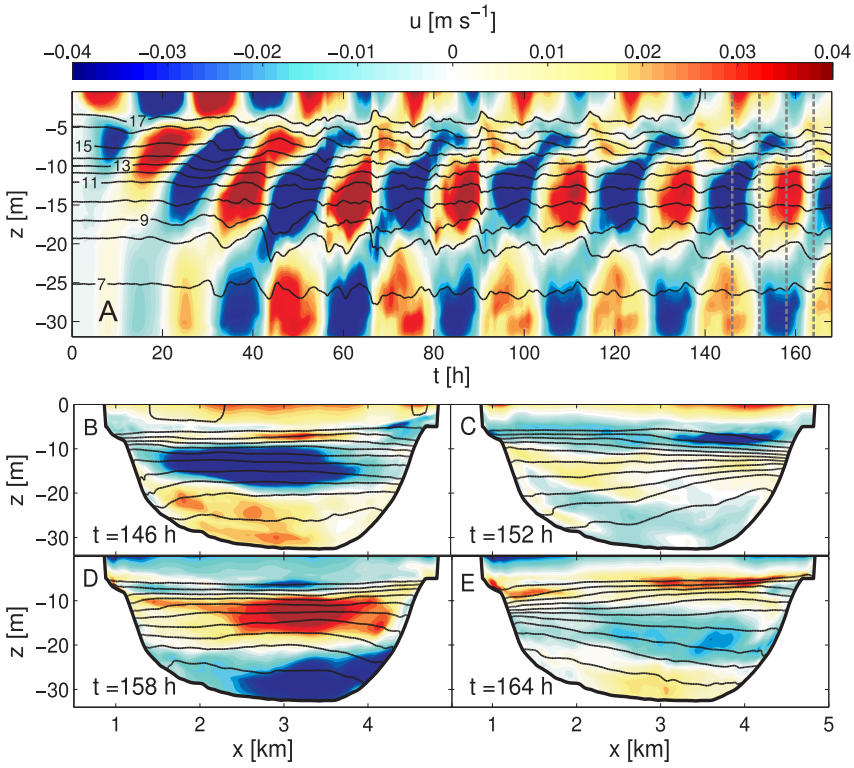

Figure 3.10: (a) Modeled isotherms (black contours, in °C), and along-basin velocities in Lake Alpnach for the case of sinusoidal diurnal wind forcing (results are shown for position C marked in Figure 3.9). Panels (b-e) show transects along the major axis of the lake (see Figure 3.9) at different times separated by $T_f/4$, as indicated by the vertical dashed lines in panel (a). Time is given in hours after the onset of the idealized wind forcing. The model was initialized with zero velocities and a measured temperature profile, assuming horizontal homogeneity. Modified figure from Becherer and Umlauf (2011).

the possibility of exchange of fluid between the BBL and the quiescent interior (Becherer and Umlauf, 2011).

The relevance of these findings for the whole basin becomes evident from Figure 3.11a,c, showing the spatial distribution of the gravitationally unstable near-bottom layers during two periods with maximum near-bottom seiching speeds. This figure reveals that during periods of up-slope flow on one of the two main slopes, respectively, shear-induced convection is observed over nearly the entire slope region below the thermocline, whereas the BBL on the opposing slope remains gravitationally stable (Becherer and Umlauf, 2011). The thickness h_{cl} of the unstable near-bottom layer may reach up to 3 m at the lower part of the slope, which was found to be in excellent agreement with the measurements by Lorke et al. (2005). The spatial distribution of the mixing rate X_b defined in (3.7) illustrates that most of the mixing is associated with the stably stratified BBLs over bottom areas with

down-slope flow, whereas the contribution of the convective regions is negligible (Figure 3.11b,d). This generalizes the results from station S3 for the whole deep-water region of the lake, leading to the important conclusions that shear-induced convection is the rule rather than the exception in this lake, and possibly also in others with similar geometry and forcing conditions.

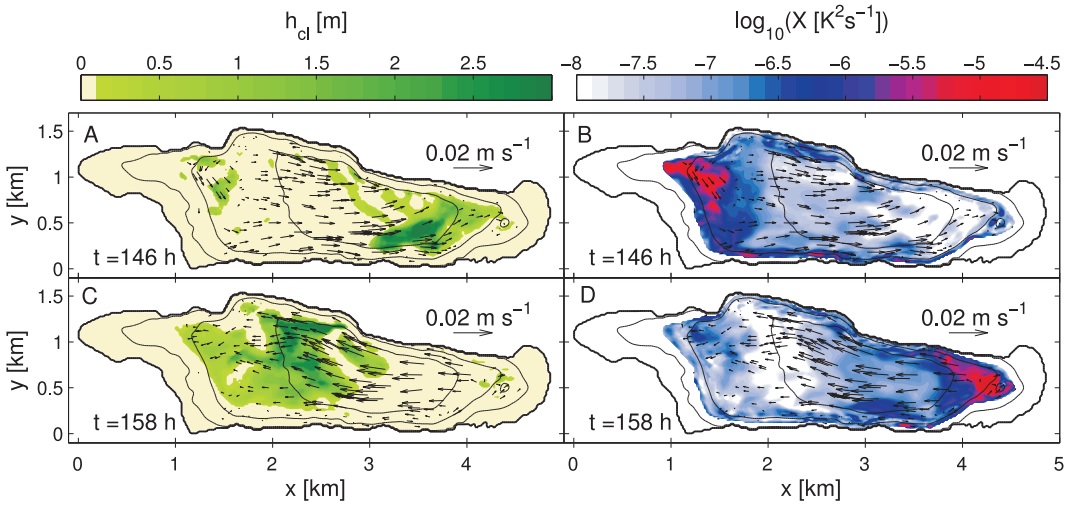

Figure 3.11: Snapshots of model results for (a,c) thickness of the near-bottom convective layer, and (b,d) mixing rate defined in (3.7). Average velocities in the BBL are indicated by arrows. Upper and lower rows correspond to the times of maximum seiching speeds along the main axis of the lake (Figure 3.10b,d show the corresponding velocity fields). Modified figure from Becherer and Umlauf (2011).

In Paper 11 by Lorrai et al. (2011), these results were extended towards cases with realistic atmospheric forcing, and compared to high-resolution velocity and stratification measurements inside the BBL: for the year 2007 at position S1 on the south-western slope, and for 2003 at position S2 at the foot of the slope (Figure 3.9). The slope measurements from 2007 were complemented by long-term current measurements in the center of the lake at position C that provided information about the vertical structure of the internal seiching motions. From a decomposition of the latter into long internal-wave modes, Lorrai et al. (2011) showed that for typical summer conditions, the dominant mode was a mixed vertical mode-2/mode-3 internal seiche with diurnal period. Comparison of model simulations and observations at positions S1 (2007) and S2 (2003) showed that both the basin-scale internal-wave field and the local response of the BBL were well represented by the model. In spite of different forcing conditions in 2003 and 2007, different stratification, and different slope angles at positions S1 and S2, gravitationally unstable BBLs could be identified in both data sets, and were reproduced with good accuracy by the model. This provided further support for the ubiquitous nature of shear-induced convection.

It has, however, also become clear from these simulations that the complex structure of shear and stratification inside the BBL requires an excessively small vertical grid spacing in the near-bottom region (of the order 0.1 m in the case of Lake Alpnach) that could only be achieved with the special zoomed and topography-following grid used in this study. As briefly discussed in Paper 10, the combination of steep slopes and high vertical resolution makes such simulations prone to so-called pressure-gradient errors that form a well-known problem in numerical models with topography-following grids (e.g., Mellor et al., 1993). In our applications, these problems could be overcome with advanced numerical schemes (Shchepetkin and McWilliams, 2003) and high horizontal resolution, both, however, associated with high computational costs. Due to the complexity of the boundary mixing processes studied here, and in view of their overwhelming importance for basin-scale mixing, there appears to be no viable alternative to this kind of numerically expensive simulations. Future limnological applications with the model used here may profit from the availability of vertically adaptive grids that have recently been developed (Hofmeister et al., 2010), and successfully applied to the gravity current studies described in Section 2.5.2 above.

3.4.2 Quantification of basin-scale mixing

In order to quantify the basin-scale effect of boundary mixing in terms of an effective diffusivity ν_{eff}, the traditional approach is based on the computation of the net vertical buoyancy flux, defined as the horizontal integral of the local vertical buoyancy flux, $-\nu_t^h N^2$, where ν_t^h is the local vertical diffusivity predicted by the turbulence model. The result is then identified with the *apparent* basin-scale flux, $-\nu_{\text{eff}} N_\infty^2 A$, where $A(z)$ denotes the hypsographic area, and $N_\infty(z)$ some representative value for the internal stratification. This yields an expression of the form

$$\nu_{\text{eff}}(z) = \frac{1}{A} \int_A \nu_t^h \frac{N^2}{N_\infty^2} \, \mathrm{d}A \, , \tag{3.8}$$

where integration is over the horizontal area of the basin at depth z (e.g., Garrett, 1990). However, as pointed out by Becherer and Umlauf (2011), this approach is not generally applicable. Taking shear-induced convection as an example, this is easily seen from the fact that unstable areas ($N^2 < 0$) result in negative contributions to the integral in (3.8), which is physically meaningless, and may even lead to a negative ν_{eff}. This is completely analogous to the one-dimensional case discussed in Section 3.3, where the mixing rate defined in (3.7), rather than the turbulent vertical buoyancy flux, was shown to be the appropriate parameter for the quantification of net mixing.

For the three-dimensional case, Becherer and Umlauf (2011) derived a generally valid expression for the effective diffusivity based on the approach suggested by Winters and D'Asaro (1996). Their method relies on a vertical sorting algorithm, in which fluid particles are assigned a new vertical position z_* such that the sorted temperature field $T(z_*, t)$ becomes

a monotonically increasing function of z_*. Winters and D'Asaro (1996) pointed out that the distribution of $T(z_*, t)$ is not affected by reversible motions like internal seiches, making it an ideal indicator for mixing. Becherer and Umlauf (2011) extended this method to their Reynolds-averaged framework, in which turbulent motions are parametrized, rather than explicitly resolved as in the original approach by Winters and D'Asaro (1996). They showed that for their simulations, where lateral turbulent fluxes are ignored, the expression for the effective diffusivity is of the form:

$$\nu_{\text{eff}}(z_*) = \frac{1}{S} \int_S \nu_t^h \left(\frac{N^2}{N_\infty^2} \right)^2 \, \mathrm{d}S \,, \tag{3.9}$$

where, different from (3.8), integration is over isothermal (or isopycnal) surfaces, and N_∞ corresponds to the stratification in the sorted state. Note that the local stratification now appears in squared form, which avoids unphysical negative contributions to the integral.

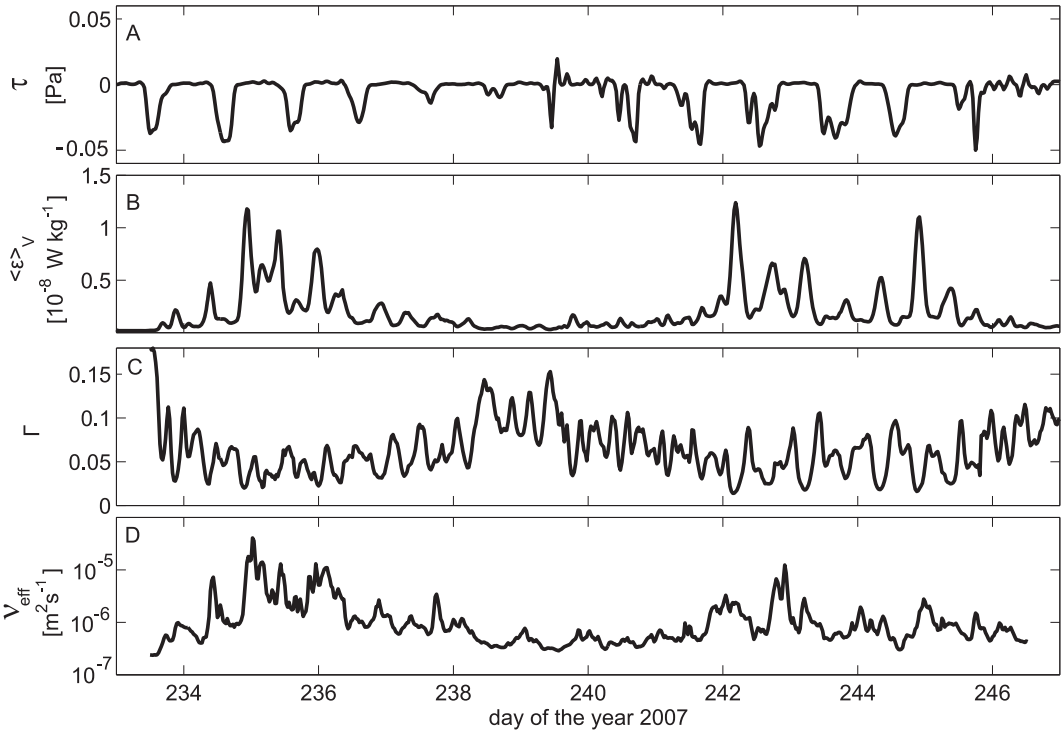

Figure 3.12: Time series of model results with realistic atmospheric forcing: (a) wind stress, (b) deep-water dissipation rate, (c) deep-water mixing efficiency, and (d) effective diffusivity at 25 m depth. The averages in (b) and (c) have been computed for the deep-water volume of the lake below 15 m depth (maximum water depth is about 34 m). Modified figure from Lorrai et al. (2011).

An application of this method for the quantification of net deep-water mixing in Lake Alpnach is illustrated in Figure 3.12, taken from Paper 11 by Lorrai et al. (2011). This figure shows the temporal evolution of a number of simulated deep-water mixing parameters

for a two-week period centered around the field campaign in 2007. The wind stress along the major axis of the lake is seen to be characterized by the diurnal thermal wind field mentioned above, super-imposed by a slower (meso-scale) modulation that leads to nearly collapsing wind speeds around day 238. The diurnal periodicity in the wind speed results in semi-diurnal fluctuations in the average deep-water dissipation rate, which simply mirrors maxima in the near-bottom velocities that appear twice per seiching cycle (Figure 3.12b). Lorrai et al. (2011) showed that the deep-water energy dissipation (and all other turbulence parameters) are dominated by the contribution of the turbulent BBL, which underlines the overwhelming importance of boundary turbulence for overall basin-scale mixing and energy dissipation.

The mixing efficiency (Figure 3.12c) is seen to be exactly anti-correlated with the semi-diurnal variability in the dissipation rate, suggesting that energetic turbulence is generally associated with smaller mixing efficiencies. Lorrai et al. (2011) pointed out that this anti-correlation is also evident on longer time scales: during the collapse of the surface wind stress around day 238, dissipation rates quickly decay, whereas mixing efficiencies increase to values of up to 15 percent (Figure 3.12c). Comparison with the one-dimensional case in Figure 3.8a illustrates that the three-dimensional simulations generally exhibit much higher mixing efficiencies. This points towards the importance of BBL restratification by exchange of fluid with the interior, which is not taken into account in the one-dimensional model. The overall effect of boundary mixing, expressed in terms of an effective basin-scale diffusivity according to (3.9), is shown in Figure 3.12c. For an intermediate depth level inside the lower layer ($z = -25$ m), ν_{eff} is seen to exhibit a variability between less than 10^{-6} m^2 s^{-1} during low winds and up to 10^{-5} m^2 s^{-1} during the periods with regular wind forcing, which Lorrai et al. (2011) showed to be in excellent agreement with available observations.

3.5 What we have learned

This study has shown that a seemingly exotic phenomenon — the shear-induced generation of gravitationally unstable BBLs during up-slope flow — turned out to be a ubiquitous feature that could be identified at all locations in the investigated lakes, as well as in numerical models of different complexity, covering a rather wide range of physical parameters. Quite surprisingly, however, in spite of the additional input of turbulent kinetic energy due to convection, the contribution of the unstable BBLs to net diapycnal mixing was found to be negligible, mainly due to the fact that convective layers are already well-mixed. During down-slope slope, when the vertical shear in the BBL is favorable for the generation of stable stratification, the picture is entirely different: the combination of energetic near-bottom turbulence and shear-induced stable stratification could be shown to result in particularly strong and efficient mixing. Overall, this effect was shown to provide the largest contribu-

tion to net basin-scale mixing, at least for the lakes and parameter range studied in this work.

The rate of mixing of small-scale buoyancy fluctuations defined in (3.7), rather than the commonly used turbulent buoyancy flux, was identified as the key parameter for the quantification of mixing, valid for both unstable and stable stratification. Using this measure for mixing, idealized one-dimensional simulations have shown that the slope angle has the most pronounced effect on the overall efficiency of boundary mixing, where steeper slopes show a stronger tendency for BBL restratification and thus yield higher efficiencies. Even for the steepest slopes, however, maximum efficiencies did not exceed a few percent in these one-dimensional simulations. Three-dimensional simulations of boundary mixing in a realistic environment were found to result in much higher mixing efficiencies (between 5 and 15 percent), suggesting that the exchange of fluid between BBL and interior, for geometric reasons not permitted in the one-dimensional simulations, forms a crucial additional mechanism for BBL restratification in lakes, and perhaps also in the ocean (see the historic discussion by Armi, 1978; Garrett, 1979; Armi, 1979). From an oceanographic point of view, this analysis is incomplete as some important effects, above all those related to rotation (see, e.g., MacCready and Rhines, 1993; Moum et al., 2004), have not been considered in sufficient detail. Work is in progress that takes these effects into account.

Chapter 4

List of papers included in this work

In the following, a brief compilation of the 11 papers constituting this thesis is provided. According to section 5 (paragraph 5) of the Habiltation Regulations of the Faculty of Mathematics and Natural Sciences at the University of Rostock, the contribution of the author has been explicitly indicated.

1. Paper 1 by Arneborg et al. (2007) contains a combined model-data study of the dynamics of dense bottom currents in the Western Baltic Sea. My contribution concerned the modeling part of this paper, including model set-up, simulations, analysis of model results, and text writing.

2. In Paper 2 by Umlauf et al. (2007), a new gravity-current data set was discussed, extending the local measurements in Paper 1 to full transects across the flow, including mixing parameters. Apart from many useful suggestions and remarks from my co-authors, I was responsible for most of the analysis and text writing.

3. In Paper 3 by Umlauf and Arneborg (2009a), an in-depth description of the full gravity-current data set from 2005 was presented, extending the preliminary discussion in Paper 2. Text writing, data analysis, and figure design have been performed largely by myself. Besides many suggestions and corrections, my coauthor contributed the analysis and discussion of the accoustic bottom stress estimates.

4. In Paper 4 by Umlauf and Arneborg (2009b), the local theory developed in Paper 1 was extended to include the full cross-channel dynamics. The theoretical work was developed together with my co-author, who also provided some of the figures and many useful comments and suggestions. Most of the text writing and data analysis, however, was contributed from my side.

5. Paper 5 by Umlauf et al. (2010) contains a two-dimensional numerical study of the cross-channel dynamics along the lines of Paper 4. My co-authors mainly contributed

with the initial model set-up and assistance with the newly developed adaptive coordinate system by Hofmeister et al. (2010). My responsibility for this work concerned most of the text writing, theory, and data analysis.

6. Paper 6 by Umlauf and Burchard (2005) contains a state-of-the-art review of second-moment turbulence models used in marine applications, including a detailed description of the models used in the central Chapters 2 and 3 of this thesis. The majority of the theoretical analysis and text writing was performed by myself, although with substantial contributions from my coauthor, who was also responsible for the larger part of the model simulations.

7. Paper 7 by Umlauf (2009) compares the performance of the second-order turbulence models discussed in Paper 6 to some flows of special interest in large-scale ocean modeling. Special focus of this paper were the mixing properties of these models in regions with vanishing vertical current shear, as they appear at the velocity maximum of some relevant flows like the equatorial undercurrent and in many bottom gravity currents.

8. Paper 8 by Lorke et al. (2008) contains the first contribution to the boundary-mixing part in this thesis, presenting evidence for the occurence of shear-induced convection in the bottom boundary layer of a large lake (Lake Constance). I contributed with the analysis of mixing data and text writing for the corresponding sections in this short paper.

9. Paper 9 by Umlauf and Burchard (2011) is a theoretical modeling study of the effect of slope-normal shear on stratification and mixing in oscillating bottom boundary layers on sloping topography. Theory, numerical simulations, their analysis, and the text writing were largely performed by myself. This paper was motivated by a suggestion of my co-author, who also provided numerous remarks and corrections during the evolution of the manuscript.

10. In Paper 10 by Becherer and Umlauf (2011), the one-dimensional and highly idealized simulations in Paper 9 were extended to a realistic three-dimensional system (Lake Alpnach, Switzerland). The modeling work was performed by the first author, Johannes Becherer, who was a master student in this project supervised by me. My contribution to this paper was the basic research idea, most of the text writing, and strong guidance regarding the analysis of the model data.

11. Paper 11 by Lorrai et al. (2011) is the companion paper to Becherer and Umlauf (2011), containing the observational component of the project, as well as a comparison to a realistic three-dimensional model. In this paper, I contributed with the modal analysis of the observed internal seiching motions, the coordination of the modeling

work (again conducted by the master student Johannes Becherer), and more than 50 percent of the text writing.

Bibliography

Appt, J., J. Imberger, and H. Kobus, 2004: Basin-scale motion in stratified Upper Lake Constance. *Limnol. Oceanogr.*, **49 (4)**, 919–933, doi:10.4319/lo.2004.49.4.0919.

Armi, L., 1978: Some evidence for boundary mixing in the deep ocean. *J. Geophys. Res.*, **83 (C4)**, 1971–1979, doi:10.1029/JC083iC04p01971.

Armi, L., 1979: Reply to comments by C. Garrett. *J. Geophys. Res.*, **84 (C8)**, 5097–5098.

Arneborg, L., V. Fiekas, L. Umlauf, and H. Burchard, 2007: Gravity current dynamics and entrainment: A process study based on observations in the Arkona Basin. *J. Phys. Oceanogr.*, **37 (8)**, 2094–2113, doi:10.1175/JPO3110.1.

Astraldi, M., G. P. Gasparini, L. Gervasio, and E. Salusti, 2001: Dense water dynamics along the Strait of Sicily (Mediterranean Sea). *J. Phys. Oceanogr.*, **31**, 3457–3475.

Baringer, M. and J. F. Price, 1997a: Mixing and spreading of the Mediterranean outflow. *J. Phys. Oceanogr.*, **27**, 1654–1677.

Baringer, M. and J. F. Price, 1997b: Momentum and energy balance of the Mediterranean outflow. *J. Phys. Oceanogr.*, **27**, 1678–1692.

Becherer, J. and L. Umlauf, 2011: Boundary mixing in lakes. 1. Modeling the effect of shear-induced convection. *J. Geophys. Res.*, **116**, C10 017, doi:10.1029/2011JC007119.

Borenäs, K., R. Hietala, J. Laaneraru, and P. Lundberg, 2007: Some estimates of the Baltic deep-water transport through the Stolpe trench. *Tellus*, **59A (2)**, 238–248, doi: 10.1111/j.1600-0870.2006.00221.x.

Burchard, H. and K. Bolding, 2002: GETM – a general estuarine transport model. Scientific documentation. Tech. Rep. EUR 20253 EN, European Commission, 157 pp.

Burchard, H., K. Bolding, T. P. Rippeth, A. Stips, J. H. Simpson, and J. Sündermann, 2001: Microstructure of turbulence in the northern North Sea: A comparative study of observations and model simulations. *J. Sea Res.*, **47**, 223–238.

Burchard, H. and R. D. Hetland, 2010: Quantifying the contributions of tidal straining and gravitational circulation to residual circulation in periodically stratified tidal estuaries. *J. Phys. Oceanogr.*, **40**, 1243–1262.

Burchard, H., F. Janssen, K. Bolding, L. Umlauf, and H. Rennau, 2009: Model simulations of dense bottom currents in the Western Baltic Sea. *Cont. Shelf Res.*, **29 (1)**, 205–220, doi:10.1016/j.csr.2007.09.010.

Burchard, H., H. U. Lass, V. Mohrholz, L. Umlauf, J. Sellschopp, V. Fiekas, K. Bolding, and L. Arneborg, 2005: Dynamics of medium-intensity dense water plumes in the Arkona Sea, Western Baltic Sea. *Ocean Dyn.*, **55**, 391–402.

Cenedese, C. and C. Adduce, 2008: Mixing in density-driven current flowing down a slope in a rotating fluid. *J. Fluid Mech.*, **604**, 369–388.

Cenedese, C. and C. Adduce, 2010: A new parameterization for entrainment in overflows. *J. Phys. Oceanogr.*, **40**, 1835–1850.

Cuthbertson, A. J. S., J. Laanerau, A. K. Wåhlin, and P. A. Davies, 2011: Experimental and analytical investigation of dense gravity currents in a rotating, up-sloping and converging channel. *Dyn. Atmos. Oceans*, **52**, 386–409.

Darelius, E., 2008: Topographic steering of dense overflows: Laboratory experiments with V-shaped ridges and canyons. *Deep Sea Res. I*, **55**, 1021–1034.

Darelius, E., I. Fer, and D. Quadfasel, 2011: Faroe Bank Channel overflow: Mesoscale variability. *J. Phys. Oceanogr.*, **41**, 2137–2154.

Darelius, E. and A. K. Wåhlin, 2007: Downward flow of dense water leaning on a submarine ridge. *Deep Sea Res. I*, **54**, 1173–1188.

Davies, P. A., A. K. Wåhlin, and Y. Guo, 2006: Laboratory and analytical model studies of the Faroe Bank Channel deep-water overflow. *J. Phys. Oceanogr.*, **36**, 1348–1364.

Ezer, T., 2006: Topographic influence on overflow dynamics: Idealized numerical simulations and the Faroe Bank Channel overflow. *J. Geophys. Res.*, **111**, C02 002, doi: 10.1029/2005JC003195.

Fer, I., 2006: Scaling turbulent dissipation in an Arctic fjord. *Deep-Sea Res. II*, **53 (1–2)**, 77–95, doi:10.1016/j.dsr2.2006.01.003.

Fer, I., U. Lemmin, and S. Thorpe, 2001: Cascading of water down the sloping sides of a deep lake in winter. *Geophys. Res. Lett.*, **28 (10)**, 2093–2096, doi:10.1029/2000GL012599.

Fer, I., R. Skogseth, and P. M. Haugan, 2004: Mixing of the Storfjorden overflow (Svalbard Archipelago) inferred from density overturns. *J. Geophys. Res.*, **109**, C01 005, doi: 10.1029/2003JC001968.

Fer, I., G. Voet, K. S. Seim, and B. Rudels, 2010: Intense mixing of the Faroe Bank Channel overflow. *Geophys. Res. Lett.*, **37**, L02 604, doi:10.1029/2009GL041924.

Foldvik, A., et al., 2004: Ice shelf water overflow and bottom water formation in the southern Weddell Sea. *J. Geophys. Res.*, **109 (C02015)**, doi:doi:10.1029/2003JC002008.

Garrett, C., 1979: Comment on 'Some evidence for boundary mixing in the deep ocean' by Laurence Armi. *J. Geophys. Res.*, **84 (C8)**, 5095–5096, doi:10.1029/JC084iC08p05095.

Garrett, C., 1990: The role of secondary circulation in boundary mixing. *J. Geophys. Res.*, **95 (C3)**, 3181–3188.

Garrett, C., P. MacCready, and P. Rhines, 1993: Boundary mixing and arrested Ekman layers: Rotating stratified flow near a sloping bottom. *Annu. Rev. Fluid Mech.*, **25**, 291–323, doi:10.1146/annurev.fl.25.010193.001451.

Gill, A. E., 1977: The hydraulics of rotating channel flow. *J. Fluid Mech.*, **80 (4)**, 641–671.

Gloor, M., A. Wüest, and D. M. Imboden, 2000: Dynamics of mixed bottom layers and its implications for diapycnal transport in a stratified, natural water basin. *J. Geophys. Res.*, **105 (C4)**, 8629–8646, doi:10.1029/1999JC900303.

Goudsmit, G.-H., F. Peeters, M. Gloor, and A. Wüest, 1997: Boundary versus internal diapycnal mixing in stratified natural waters. *J. Geophys. Res.*, **102 (C13)**, 27 903–27 914, doi:10.1029/97JC01861.

Hofmeister, R., H. Burchard, and J.-M. Beckers, 2010: Non-uniform adaptive vertical grids for 3D numerical ocean models. *Ocean Modelling*, **33 (1–2)**, 70–86, doi:10.1016/j.ocemod.2009.12.003.

Hogg, N. G., 1983: Hydraulic control and flow separation in a multi-layered fluid with applications to the Vema Channel. *J. Phys. Oceanogr.*, **13**, 695–708.

Holtermann, P. and L. Umlauf, 2012: The Baltic Sea Tracer Release Experiment. 2. Mixing processes. *J. Geophys. Res.*, **117**, C01 022, doi:10.1029/2011JC007445.

Holtermann, P., L. Umlauf, T. Tanhua, O. Schmale, G. Rehder, and J. Waniek, 2012: The Baltic Sea Tracer Release Experiment. 1. Mixing rates. *J. Geophys. Res.*, **117**, C01 021, doi:10.1029/2011JC007439.

Hughes, G. O. and R. W. Griffiths, 2006: A simple convective model of the global overturning circulation including effects of entrainment into sinking regions. *Ocean Modelling*, **12**, 46–79.

Ilıcak, M., S. Legg, A. Adcroft, and R. Hallberg, 2011: Dynamics of a dense gravity current flowing over a corrugation. *Ocean Modelling*, **38 (1–2)**, 71–84, doi:10.1016/j.ocemod.2011.02.004.

Jay, D. A. and J. D. Musiak, 1994: Particle trapping in estuarine tidal flows. *J. Geophys. Res.*, **99 (C10)**, 20 445–20 461.

Johnson, G. C., R. G. Lueck, and T. B. Sanford, 1994a: Stress on the Mediterranean outflow plume: Part II. Dissipation and shear measurements. *J. Phys. Oceanogr.*, **24**, 2084–2092.

Johnson, G. C. and D. R. Ohlsen, 1994: Frictionally modified rotating hydraulic channel exchange and ocean outflows. *J. Phys. Oceanogr.*, **24**, 66–75.

Johnson, G. C. and T. B. Sanford, 1992: Secondary circulation in the Faroe Bank channel outflow. *J. Phys. Oceanogr.*, **22**, 927–933.

Johnson, G. C., T. B. Sanford, and M. O. Baringer, 1994b: Stress on the Mediterranean outflow plume: Part I. Velocity and water property measurements. *J. Phys. Oceanogr.*, **24**, 2072–2083.

Kämpf, J., 2000: Impact of multiple submarine channels on the descent of dense water at high latitudes. *J. Geophys. Res.*, **105**, 8753–8773.

Killworth, P. D., 1992: Flow properties in rotating, stratified hydraulics. *J. Phys. Oceanogr.*, **22**, 997–1017.

Killworth, P. D., E. C. Carmack, R. F. Weiss, and R. Matear, 1996: Modeling deep-water renewal in Lake Baikal. *Limnol. Oceanogr.*, **41 (7)**, 1521–1538.

Kunze, E., C. MacKay, E. McPhee-Shaw, K. Morrice, J. Girton, and S. Terker, 2012: Turbulent mixing and exchange with interior waters on sloping boundaries. *J. Phys. Oceanogr.*, doi:10.1175/JPO-D-11-075.1, in press.

Lake, I., K. Borenäs, and P. Lundberg, 2005: Potential-vorticity characteristics of the Faroe Bank Channel deep-water overflow. *J. Phys. Oceanogr.*, **35**, 921–932.

Ledwell, J. R. and B. M. Hickey, 1995: Evidence for enhanced boundary mixing in the Santa Monica Basin. *J. Geophys. Res.*, **100 (C10)**, 20 665–20 679, doi:10.1029/94JC01182.

Ledwell, J. R., E. T. Montgomery, K. L. Polzin, L. C. St. Laurent, R. W. Schmitt, and J. M. Toole, 2000: Evidence for enhanced mixing over rough topography in the abyssal ocean. *Nature*, **403 (6766)**, 179–182, doi:10.1038/35003164.

Ledwell, J. R., A. J. Watson, and C. S. Law, 1993: Evidence for slow mixing across the pycnocline from an open-ocean tracer-release experiment. *Nature*, **364**, 701–703.

Liang, L. and R. W. Garwood, 1998: Effects of topographic steering and ambient stratification on overflows on continental slopes: A model study. *J. Geophys. Res.*, **103**, 5459–5476.

Lorke, A., V. Mohrholz, and L. Umlauf, 2008: Stratification and mixing on sloping boundaries. *Geophys. Res. Lett.*, **35 (L14610)**, doi:10.1029/2008GL034607.

Lorke, A., F. Peeters, and A. Wüest, 2005: Shear-induced convective mixing in bottom boundary layers on slopes. *Limnol. Oceanogr.*, **50 (5)**, 1612–1619.

Lorke, A., L. Umlauf, T. Jonas, and A. Wüest, 2002: Dynamics of turbulence in low-speed oscillating bottom boundary-layers of stratified basins. *Environ. Fluid Mech.*, **2**, 291–313.

Lorrai, C., L. Umlauf, J. Becherer, A. Lorke, and A. Wüest, 2011: Boundary mixing in lakes. 2. Combined effects of shear-induced and convective turbulence on basin-scale mixing. *J. Geophys. Res.*, **116**, C10 018, doi:10.1029/2011JC007121.

Lundberg, P., 1983: On the mechanics of the deep-water flow in the Bornholm Channel. *Tellus*, **35A**, 149–158.

MacCready, P. and P. B. Rhines, 1993: Slippery bottom boundary layers on a slope. *J. Phys. Oceanogr.*, **23**, 5–22.

Mauritzen, C., J. Price, T. Sanford, and D. Torres, 2005: Circulation and mixing in the Faroese channels. *Deep-Sea Res. I*, **52**, 883–913.

Meier, H. E. M., 2007: Modeling the pathways and ages of inflowing salt- and freshwater in the Baltic Sea. *Estuarine, Coastal and Shelf Science*, **74 (4)**, 610–627.

Meier, H. E. M., et al., 2006: Ventilation of the Baltic Sea deep water: A brief review of present knowledge from observations and models. *Oceanologia*, **48**, 133–164.

Mellor, G. L., T. Ezer, and L.-Y. Oey, 1993: The pressure gradient conundrum of sigma coordinate ocean models. *J. Atmos. Ocean. Tech.*, **11**, 1126–1135.

Moum, J. N., A. Perlin, K. Klymak, M. D. Levine, and T. Boyd, 2004: Convectively-driven mixing in the bottom boundary layer. *J. Phys. Oceanogr.*, **34 (10)**, 2189–2202, doi:10.1175/1520-0485(2004)034<42189:CDMITB>2.0.CO;2.

Munk, W. and C. Wunsch, 1998: Abyssal recipes II: Energetics of tidal and wind mixing. *Deep-Sea Res. I*, **45 (12)**, 1977–2010, doi:10.1016/S0967-0637(98)00070-3.

Munk, W. H., 1966: Abyssal recipes. *Deep-Sea Res.*, **13 (4)**, 707–730, doi:10.1016/0011-7471(66)90602-4.

Münnich, M., A. Wüest, and D. M. Imboden, 1992: Observations of the second vertical mode of the internal seiche in an alpine lake. *Limnol. Oceanogr.*, **37 (8)**, 1705–1719.

Nash, J. D., M. H. Alford, E. Kunze, K. Martini, and S. Kelly, 2007: Hotspots of deep ocean mixing on the Oregon continental slope. *Geophys. Res. Lett.*, **34**, L01 605, doi:10.1029/2006GL028170.

Osborn, T. R., 1980: Estimates of the local rate of vertical diffusion from dissipation measurements. *J. Phys. Oceanogr.*, **10 (1)**, 83–89, doi:10.1175/1520-0485(1980)010<0083:EOTLRO>2.0.CO;2.

Paka, V. T., V. M. Zhurbas, N. N. Golenko, and L. A. Stefantsev, 1998: Effect of the Ekman transport on the overflow of saline waters through the Slupsk Furrow in the Baltic Sea. *Izvestiya Atmospheric and Oceanic Phyiscs*, **34 (5)**, 641–648, translated version.

Perlin, A., J. N. Moum, J. M. Klymak, M. D. Levine, T. Boyd, and P. M. Kosro, 2005: A modified law of the wall to describe velocity profiles in the oceanic bottom boundary layers. *J. Geophys. Res.*, **110 (C10S10)**, doi:10.1029/2004JC002 310.

Perlin, A., J. N. Moum, J. M. Klymak, M. D. Levine, T. Boyd, and P. M. Kosro, 2007: Ogranization of stratification, turbulence, and veering in bottom Ekman layers. *J. Geophys. Res.*, **112 (C05S90)**, doi:10.1029/2004JC002 641.

Peters, H. and W. E. Johns, 2005: Mixing and entrainment in the Red Sea outflow plume. II. Turbulence characteristics. *J. Phys. Oceanogr.*, **35**, 584–600.

Peters, H. and W. E. Johns, 2006: Bottom layer turbulence in the Red Sea outflow plume. *J. Phys. Oceanogr.*, **36**, 1763–1785.

Peters, H., W. E. Johns, A. S. Bower, and D. M. Fratantoni, 2005: Mixing and entrainment in the Red Sea outflow plume. I. Plume structure. *J. Phys. Oceanogr.*, **35**, 569–583.

Petrén, O. and G. Walin, 1976: Some observations of the deep flow in the Bornholm strait during the period June 1973–December 1974. *Tellus*, **28**, 74–87.

Phillips, O. M., 1970: On flows induced by diffusion in a stably stratified fluid. *Deep-Sea Res.*, **17**, 435–443.

Polzin, K. L., J. M. Toole, J. R. Ledwell, and R. W. Schmitt, 1997: Spatial variability of turbulent mixing in the abyssal ocean. *Science*, **276**, 93–96.

Pratt, L. J., 1986: Hydraulic control of sill flow with bottom friction. *J. Phys. Oceanogr.*, **16**, 1970–1980.

Pratt, L. J., 2004: Recent progress on understanding the effect of rotation in models of sea straits. *Deep-Sea Res. II*, **51**, 351–369.

Pratt, L. J. and P. A. Lundberg, 1991: Hydraulics of rotating strait and sill flow. *Ann. Rev. Fluid Mech.*, **23**, 81–106.

Reissmann, J., et al., 2009: Vertical mixing in the Baltic Sea and consequences for eutrophication – A review. *Progr. Oceanogr.*, **82 (1)**, 47–80, doi:10.1016/j.pocean.2007.10.004.

Rudnick, D. L., et al., 2003: From Tides to Mixing Along the Hawaiian Ridge. *Science*, **301 (5631)**, 355–357, doi:10.1126/science.1085837.

Seim, K. S. and I. Fer, 2011: Mixing in the stratified interface of the Faroe Bank Channel overflow: The role of transverse circulation and internal waves. *J. Geophys. Res.*, **116**, C07 022, doi:10.1029/2010JC006805.

Sellschopp, J., et al., 2006: Direct observations of a medium-intensity inflow into the Baltic Sea. *Cont. Shelf Res.*, **26 (19)**, 2393–2414, doi:10.1016/j.csr.2006.07.004.

Shchepetkin, A. F. and J. C. McWilliams, 2003: A method for computing horizontal pressure-gradient force in an oceanic model with a nonaligned vertical coordinate. *J. Geophys. Res.*, **108 (C3)**, 3090, doi:10.1029/2001JC001.

Sherwin, T. J., C. R. Griffiths, M. E. Inall, and W. R. Turrell, 2008: Quantifying the overflow across the Wyville Thomson Ridge. *Deep-Sea Res.*, **55**, 396–404.

Simpson, J. H., J. Brown, J. Matthews, and G. Allen, 1990: Tidal straining, density currents, and stirring in the control of estuarine stratification. *Estuaries and Coasts*, **13**, 125–132.

Smith, P. C., 1975: A streamtube model for bottom boundary currents in the ocean. *Deep-Sea Res.*, **22**, 853–873.

Taylor, J. R. and S. Sarkar, 2008: Stratification effects in a bottom Ekman layer. *J. Phys. Oceanogr.*, **38**, 2535–2555, doi:10.1175/2008JPO3942.1.

Tennekes, H. and J. L. Lumley, 1972: *A First Course in Turbulence*. MIT Press, Cambridge M.A., USA.

Thorpe, S. A., 1987: Current and temperature variability on the contintental slope. *Philos. Trans. Roy. Soc. London*, **A323**, 471–517.

Toole, J. M., K. L. Polzin, and R. W. Schmitt, 1994: Estimates of diapycnal mixing in the abyssal ocean. *Science*, **264 (5164)**, 1120–1123, doi:10.1126/science.264.5162.1120.

Turner, J. S., 1986: Turbulent entrainment: the development of the entrainment assumption, and its applications to geophysical flows. *J. Fluid Mech.*, **173**, 431–471.

Umlauf, L., 2009: A note on the description of mixing in stratified layers without shear in large-scale ocean models. *J. Phys. Oceanogr.*, **39**, 3032–3039.

Umlauf, L. and L. Arneborg, 2009a: Dynamics of rotating shallow gravity currents passing through a channel. Part I: Observation of transverse structure. *J. Phys. Oceanogr.*, **39 (10)**, 2385–2401, doi:10.1175/2009JPO4159.1.

Umlauf, L. and L. Arneborg, 2009b: Dynamics of rotating shallow gravity currents passing through a channel. Part II: Analysis. *J. Phys. Oceanogr.*, **39 (10)**, 2402–2416, doi:10.1175/2009JPO4164.1.

Umlauf, L., L. Arneborg, H. Burchard, V. Fiekas, H.-U. Lass, V. Mohrholz, and H. Prandke, 2007: Transverse structure of turbulence in a rotating gravity current. *Geophys. Res. Lett.*, **34 (L08601)**, doi:10.1029/2007GL029521.

Umlauf, L., L. Arneborg, R. Hofmeister, and H. Burchard, 2010: Entrainment in shallow rotating gravity currents: A modeling study. *J. Phys. Oceanogr.*, **40 (8)**, 1819–1834, doi:10.1175/2010JPO4367.1.

Umlauf, L. and H. Burchard, 2005: Second-order turbulence closure models for geophysical boundary layers. A review of recent work. *Cont. Shelf Res.*, **25**, 795–827.

Umlauf, L. and H. Burchard, 2011: Diapycnal transport and mixing efficiency in stratified boundary layers near sloping topography. *J. Phys. Oceanogr.*, **41 (2)**, 329–345, doi:10.1175/2010JPO4438.1.

Umlauf, L., H. Burchard, and K. Bolding, 2005: GOTM – Scientific Documentation. Version 3.2. Marine Science Reports 63, Leibniz-Institute for Baltic Sea Research, Warnemünde, Germany.

van der Lee, E. M. and L. Umlauf, 2011: Internal-wave mixing in the Baltic Sea: Near-inertial waves in the absence of tides. *J. Geophys. Res.*, **116**, C10 016, doi: 10.1029/2011JC007072.

Wåhlin, A. K., 2002: Topographic steering of dense currents with application to submarine canyons. *Deep-Sea Res. I*, **49**, 305–320.

Wåhlin, A. K., 2004: Downward channeling of dense water in topographic corrugations. *Deep-Sea Res. I*, **51**, 577–590.

Wåhlin, A. K. and C. Cenedese, 2006: How entraining density currents influence the stratification in a one-dimensional ocean basin. *Deep-Sea Res. II*, **53 (1–2)**, 172–193, doi: 10.1016/j.dsr2.2005.10.019.

Wåhlin, A. K., E. Darelius, C. Cenedese, and G. F. Lane-Serff, 2008: Laboratory observations of enhanced entrainment in dense overflows in the presence of submarine canyons and ridges. *Deep-Sea Res. I*, **55**, 737–750.

Wain, D. J. and C. R. Rehmann, 2010: Transport by an intrusion generated by boundary mixing in a lake. *Water Resour. Res.*, **46**, W08 517, doi:10.1029/2009WR008391.

Wells, M. G., C. Cenedese, and C. P. Caulfield, 2010: The relationship between flux coefficient and entrainment ratio in density current. *J. Phys. Oceanogr.*, **40**, 2713–2727.

Wesson, J. C. and M. C. Gregg, 1994: Mixing at Camarinal Sill in the Strait of Gibraltar. *J. Geophys. Res.*, **99 (C5)**, 9847–9878.

Winters, K. B. and E. A. D'Asaro, 1996: Diascalar flux and the rate of fluid mixing. *J. Fluid Mech.*, **317**, 179–193, doi:10.1017/S0022112096000717.

Wüest, A. and A. Lorke, 2003: Small-scale hydrodynamics in lakes. *Annu. Rev. Fluid Mech.*, **35**, 373–412, doi:10.1146/annurev.fluid.35.101101.161220.

Wüest, A., G. Piepke, and D. Van Senden, 2000: Turbulent kinetic energy balance as a tool for estimating vertical diffusivity in wind-forced stratified waters. *Limnol. Oceanogr.*, **45 (6)**, 1388–1400, doi:10.4319/lo.2000.45.6.1388.

Wüest, A., T. M. Ravens, N. G. Granin, O. Kocsis, M. Schurter, and M. Sturm, 2005: Cold intrusions in Lake Baikal: Direct observational evidence for deep-water renewal. *Limnol. Oceanogr.*, **50 (1)**, 184–196, doi:10.4319/lo.2000.45.6.1388.

Wunsch, C. and R. Ferrari, 2004: Vertical mixing, energy, and the general circulation of the oceans. *Annu. Rev. Fluid Mech.*, **36**, 281–314, doi:10.1146/annurev.fluid.36.050802.122121.

Zhurbas, V. M., J. Elken, V. T. Paka, J. Piechura, G. Väli, I. P. Chubarenko, N. Golenko, and S. Shchuka, 2012: Structure of unsteady overflow in the Słupsk-Furrow of the Baltic Sea. *J. Geophys. Res.*, **117 (C04027)**, doi:10.1029/2011JC007284.